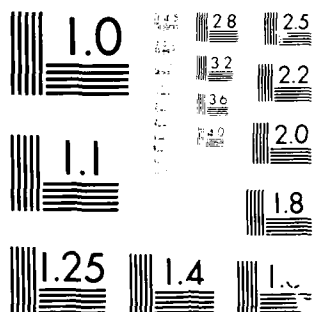


AD-A192 040 ACCURATE PROSPECTIVE AERODYNAMIC SIMULATION ON PATCHED 1/1  
MESH SYSTEMS (U) FED-X CORP TELD-AERO-CR  
C R LOMBARDO ET AL. 30 NOV 87 AFOSR-IR-88-0185  
UNCLASSIFIED F49620-85-C-0001 P/G 12/3 NL





Mitsubishi Electric Corporation  
Mitsubishi Electric America, Inc.

UNCLASSIFIED

DTIC FILE COPY

AD-A192 040

## REPORT DOCUMENTATION PAGE

1a. REPORT SECURITY CLASSIFICATION UNCLASSIFIED			1b. RESTRICTIVE MARKINGS														
2a. SECURITY CLASSIFICATION AUTHORITY <b>SELECTED</b>			3. DISTRIBUTION/AVAILABILITY OF REPORT Approved for public release; distribution unlimited.														
2b. DECLASSIFICATION/DOWNGRADING SCHEDULE SAR 01 1988			5. MONITORING ORGANIZATION REPORT NUMBER(S) <b>AFOSR-TR-88-0185</b>														
4. PERFORMING ORGANIZATION REPORT NUMBER(S) <b>CDH</b>		6a. NAME OF PERFORMING ORGANIZATION PEDA Corporation			6b. OFFICE SYMBOL (If applicable)												
6c. ADDRESS (City, State and ZIP Code) 4151 Middlefield Road, Suite 7 Palo Alto, CA 94303			7a. NAME OF MONITORING ORGANIZATION Air Force Office of Scientific Research														
8a. NAME OF FUNDING/SPONSORING ORGANIZATION AFOSR		8b. OFFICE SYMBOL (If applicable) NM			9. PROCUREMENT INSTRUMENT IDENTIFICATION NUMBER F49620-85-C-0081												
8c. ADDRESS (City, State and ZIP Code) Bolling AFB DC 20332-6448			10. SOURCE OF FUNDING NOS. <table border="1"> <tr> <td>PROGRAM ELEMENT NO. 61102F</td> <td>PROJECT NO. 2304</td> <td>TASK NO. A3</td> <td>WORK UNIT NO.</td> </tr> </table>			PROGRAM ELEMENT NO. 61102F	PROJECT NO. 2304	TASK NO. A3	WORK UNIT NO.								
PROGRAM ELEMENT NO. 61102F	PROJECT NO. 2304	TASK NO. A3	WORK UNIT NO.														
11. TITLE (Include Security Classification) Accurate, Productive Aerodynamic Simulation on Patched Mesh Systems																	
12. PERSONAL AUTHOR(S) C.K. Lombard, Joseph Olinger, Jorge Bardina, Ethiraj Venkatapathy and J.Y. Yang																	
13a. TYPE OF REPORT Annual		13b. TIME COVERED FROM 86 10 01 TO 87 09 30		14. DATE OF REPORT (Yr., Mo., Day) 87 11 30													
15. PAGE COUNT 61																	
16. SUPPLEMENTARY NOTATION																	
17. COSATI CODES <table border="1"> <tr> <th>FIELD</th> <th>GROUP</th> <th>SUB. GR.</th> </tr> <tr> <td></td> <td></td> <td></td> </tr> <tr> <td></td> <td></td> <td></td> </tr> <tr> <td></td> <td></td> <td></td> </tr> </table>			FIELD	GROUP	SUB. GR.										18. SUBJECT TERMS (Continue on reverse if necessary and identify by block number) Adaptive Gridding, CSCM, ENO Schemes, Navier-Stokes, Patched Grids, Upwind Methods.		
FIELD	GROUP	SUB. GR.															
19. ABSTRACT (Continue on reverse if necessary and identify by block number)  In the first year of a planned three year program the research has aimed at defining data structures and completing tools for a new flexible approach to scientific programming and problem solving. Both problems of program complexity associated with changing models and physics as well as joined and disjoint multiple independent patched domain decompositions for treating complex geometries can be systematically organized within the context of the directed graph programming concept being explored. Problems and parts of problems having geometric connectivity or its analogs such as precedence relationships are naturally exhibited and easily debugged or modified in the graph. The solution of problems is literally to traverse the graph. For the planned prototype aerodynamic simulation facility the graphs which are to embody grid generation and Navier-Stokes solution procedures are to be constructed with a graphical editor hosted in a high performance graphics workstation.																	
20. DISTRIBUTION/AVAILABILITY OF ABSTRACT UNCLASSIFIED/UNLIMITED <input checked="" type="checkbox"/> SAME AS RPT. <input type="checkbox"/> DTIC USERS <input type="checkbox"/>			21. ABSTRACT SECURITY CLASSIFICATION UNCLASSIFIED														
22a. NAME OF RESPONSIBLE INDIVIDUAL Major John P. Thomas, Jr., USAF			22b. TELEPHONE NUMBER (Include Area Code) (202) 767-5026		22c. OFFICE SYMBOL NM												

UNCLASSIFIED

SECURITY CLASSIFICATION OF THIS PAGE

19. Abstract cont.

The efficient global data structure for the system is a set of large linear arrays in which the data for the independent quadrilateral blocks of mesh are sequentially stacked. The directed graph is to control procedures that fill pointer arrays to the data structure. We implement both upwind characteristics based implicit computed boundary point procedures for physical and external domain boundaries and on internal patch boundaries frozen boundary data that is obtained from the solution on adjoining overlapping meshes. The approach admits segmented grids with steps and holes and boundary conditions that are nonhomogeneous by type.

Additions and improvements to our upwind computational tools have included the means to carry out resolution enhancing flow structure adaptive regridding on systems of independent patched mesh. A new essentially non oscillatory (ENO) scheme has been developed to improve the nonlinear stability of second order methods while maintaining accuracy throughout. Nonlinear stability at captured shocks has been improved by the addition of a conditioning matrix contribution to the left hand side that tends to freeze through transitions characteristics with zero eigenvalues. Finally a new more consistent upwind splitting and differencing scheme has been constructed for CSCM on biased upwind computational cell's. The new scheme features a two tier complete data staggard grid structure that has significant accuracy/data storage ratio advantages.

UNCLASSIFIED

SECURITY CLASSIFICATION OF THIS PAGE

**AFOSR-TR- 88-0185**

**Accurate, Productive Aerodynamic Simulation  
on Patched Mesh Systems**

**Annual Report  
F49620-85-C-0081  
01 Oct 1986 through 30 Sept 1987**

**Charles K. Lombard  
Principal Investigator  
PEDA Corporation**

**88 2 25 084**

## **Accurate, Productive Aerodynamic Simulation on Patched Mesh Systems**

**C.K. Lombard, Joseph Oliger,  
Jorge Bardina, Ethiraj Venkatapathy and J.Y. Yang**

### **Abstract**

In the first year of a planned three year program the research has aimed at defining data structures and completing tools for a new flexible approach to scientific programming and problem solving. Both problems of program complexity associated with changing models and physics as well as joined and disjoint multiple independent patched domain decompositions for treating complex geometries can be systematically organized within the context of the directed graph programming concept being explored. Problems and parts of problems having geometric connectivity or its analogs such as precedence relationships are naturally exhibited and easily debugged or modified in the graph. The solution of problems is literally to traverse the graph. For the planned prototype aerodynamic simulation facility the graphs which are to embody grid generation and Navier-Stokes solution procedures are to be constructed with a graphical editor hosted in a high performance graphics workstation.

The efficient global data structure for the system is a set of large linear arrays in which the data for the independent quadrilateral blocks of mesh are sequentially stacked. The directed graph is to control procedures that fill pointer arrays to the data structure. We implement both upwind characteristics based implicit computed boundary point procedures for physical and external domain boundaries and on internal patch boundaries frozen boundary data that is obtained from the solution on adjoining overlapping meshes. The approach admits segmented grids with steps and holes and boundary conditions that are nonhomogeneous by type.

Additions and improvements to our upwind computational tools have included the means to carry out resolution enhancing flow structure adaptive regridding on systems of independent patched mesh. A new essentially non oscillatory (ENO) scheme has been developed to improve the nonlinear stability of second order methods while maintaining accuracy throughout. Nonlinear stability at captured shocks has been improved by the addition of a conditioning matrix contribution to the left hand side that tends to freeze through transitions characteristics with zero eigenvalues. Finally a new more consistent upwind splitting and differencing scheme has been constructed for CSCM on biased upwind computational cells. The new scheme features a two tier complete data staggard grid structure that has significant accuracy/data storage ratio advantages.



<b>Accession For</b>	
NTIS GRA&I	<input checked="" type="checkbox"/>
DTIC TAB	<input type="checkbox"/>
Unannounced	<input type="checkbox"/>
<b>Justification</b>	
By _____	
Distribution/ _____	
<b>Availability Codes</b>	
Avail and/or	
Dist	Special
A-1	

## 1. Introduction

As major strides have been made in the past several years in the speed and memory of computers, similar advances have been achieved in details of computational technique for constructing finite difference meshes and for solving the compressible Euler or Navier-Stokes equations. The combined progress has been such that the CFD community is now challenged by the possibility of solving whole interacting flows of multicomponent systems. Topical examples are flows about aircraft and missiles, and in turbomachines and rocket engines.

Such thinking is symptomatic of the fact that the research focus is rapidly shifting from 2-D explorations and demonstrations to viable 3-D computational methodologies.

The shift poses two research challenges. The first is to bring a new generation of algorithms to an effective fruition in terms of accuracy and computational efficiency. The second is to organize the problems of constructing meshes and solving the gasdynamic PDE's on geometrically complex flow domains in such a way as to minimize the work of problem setup and execution for each new geometry or mesh structure. This requires the development of computational systems to unify the many components of the simulation – principally grid generation, computation and graphics.

The present program contains both the above aspects in research aimed at substantially enhancing accuracy and productivity in the numerical simulation of aerodynamic flows in complex geometry. The program builds on and extends recent work in algebraic grid generation<sup>1-3</sup> for composite patched mesh systems and the CSCM upwind implicit algorithm<sup>4-9</sup> for solving the compressible Euler and Navier-Stokes equations. With the conservative upwind method we have successfully demonstrated<sup>10</sup> the capability to accurately capture weak reflecting shocks in compressible flow using solution adaptive grid refinement strategies with aligned overset mesh patches like those proposed by Berger and Oliger<sup>11</sup>. On conventional grids, the implicit upwind method exhibits robust stability properties with well posed implicit characteristic procedures<sup>4</sup> at all external flow boundaries. However, the upwind method particularly excels in accuracy and stability in the vicinity of interior overset patch boundaries with only a minimal overlap as required to exchange data through interpolation<sup>6</sup>.

The combined strategy of employing upwind methods with both composite and overset patched meshes is sufficient to treat problems of any geometric and flow structure complexity with desired accuracy and computational efficiency.

Mesh generators and flow solvers can be programmed<sup>11,12</sup> in FORTRAN with a flexible global data structure comprising a linear array with pointers and parameter controlled boundary interface routines to handle general multiple mesh decompositions of the domain. However, both the programming of the codes and the setup to solve particular complex problems is tedious and invites mistakes that may be hard to track down. The problems are inherent in the unnatural structure of linear programming languages like FORTRAN that do not exhibit the connectivity of objects.

Recent research by Oliger and his students has supported the possibility to write programs and execute them in a more natural way that directly represents the connectivity of objects. The approach is based on the directed graph which is to be implemented and exhibited in a workstation based graphical interface. The graph is a natural representation of the macro data flow of the program. An important feature of the system is that it is recursive, i.e. nodes of the graph may represent pieces of the graph. To facilitate using programs with disparate data structures, filters are inserted between nodes to reformat the output (range) data of one process to be suitable for the input (domain) of the next. A language such as LIL, proposed by Goguen<sup>13</sup>, is being developed for writing these filters. To minimize programming while permitting great flexibility, programming will be carried out and programs executed in the context of the UNIX environment. The Make facility of UNIX naturally lends itself to achieve the composition of these programs.

Based in the above technologies, a major purpose of the evolving program will be to construct and test a prototype programming system for aerodynamic simulation. The simulation will generate multiple patch meshes for representative problems and direct the flow solver over the meshes.

Other complementary facets of the research are to seek further improvements in accuracy and efficiency of the upwind method and algebraic grid generation procedures that we have been studying.

Topics that we are pursuing in the upwind methods area that derive from our recent research are, first, strongly conservative schemes with second order spatial accuracy in the complete 2-D and 3-D Taylor series' expansion. Here, second, these schemes are expressed in available families of upwind biased finite volume computational cells rather than the classical data node centered cells. On such cells an interesting hierarchy of splittings and biased upwind methods are possible that are related to and extend the locally one dimensional higher order TVD schemes of Chakravarthy and Osher<sup>14</sup> and Harten<sup>15</sup>. Related flux limiting schemes including some based on the work of Yang, et al.<sup>8</sup> are to be explored.

Another research topic we are embracing and one that has recently shown great promise, particularly for steady flow implementation with upwind schemes<sup>9</sup>, is flow structure adaptive mesh redistribution. This technique requires no additional patches of mesh (with additional computational costs) to achieve the same order of magnitude improvement in resolution<sup>10</sup> as is achieved with mesh embedding and overset refinement.

Topics in the algebraic grid generation area emphasize extension to 3-D. One important facet is the construction of smooth body conforming surface patches of curvilinear coordinate mesh. Our present mesh generation philosophy, which is suitable for both 2-D and 3-D, emphasizes techniques based on low order polynomial blending of parametric cubic and tension spline functions. These are used for both bounding and coordinate curves. Blended stretching functions are used to obtain desired mesh point distributions. The approach<sup>2</sup> represents a simplification of, and borrows many tools from, the transfinite interpolation method of Vinokur and Lombard<sup>1</sup>. The latter relates to the work of

Eriksson<sup>16</sup> and to Eiseman and Smith<sup>17</sup>. For boundary surface meshes, our approach which suppresses the explicit dependence on boundary gradients of Hermite interpolation follows the work of Gordon<sup>18</sup>.

Another development of the boundary blending philosophy which we are pursuing is patched mesh generation using isoparametric macro finite elements (Baker and Manhardt<sup>19</sup>). The basis functions for the elements can then be used for coordinate transformation (Mitchell and Wait<sup>20</sup>). A feature of the macro element approach which has recently been advanced in 2-D by Oliger and Suhr<sup>3</sup> is the use of piecewise quadratics for boundary curves in a way that achieves C<sup>1</sup> continuity.

An important topic of the new programming system that we are presently studying is how to represent the algebraic grid generation problem for composite meshes in a directed graph in such a way that the connectivity (continuity properties) are elicited and the procedure is made very efficient. A similar topic exists for gasdynamics in how to efficiently direct the operationally explicit symmetric Gauss-Seidel implicit solution algorithm on the composite mesh.

Finally, as suggested above, computer graphics naturally fits within the context of a complete simulation system. From an earlier effort we have a 2-D graphics package programmed in a flexible multiple mesh data structure to mirror that of the solution procedure<sup>12</sup>.

In the following sections we provide additional details about the implementation of the directed graph based programming environment and advances in computational methods that we have made.

#### References

1. Vinokur, Marcel and Lombard, C.K.: "Algebraic Grid Generation with Corner Singularities," *Advances in Grid Generation*, Vol. 5, Sponsored by ASME Fluids Engineering Div., Symposium on Grid Generation, 1983, ASME Fluids Engineering Conference, Houston TX.
2. Luh, R. C.-C., Nagaraj, N. and Lombard, C.K.: "Simplified Algebraic Grid Generation in Patched Mesh Systems," AIAA-87-0200, 1987.
3. Oliger, J. and Suhr, S.: "Component Grid Generation Using Isoparametric Macro Elements," to appear.
4. Lombard, C.K., Bardina, J., Venkatapathy, E. and Oliger, J.: "Multi-Dimensional Formulation of CSCM - An Upwind Flux Difference Eigenvector Split Method for the Compressible Navier-Stokes Equations," AIAA-83-1895, July 1983.
5. Lombard, C.K. and Venkatapathy, Ethiraj: "Implicit Boundary Treatment for Joined and Disjoint Patched Mesh Systems," AIAA 85-1503-CP, AIAA 7th Computational Fluid Dynamics Conference, Cincinnati, Oh, July 1985.
6. Bardina, Jorge and Lombard, C.K.: "Three Dimensional CSCM Method for the Compressible Navier-Stokes Equations with Application to a Multi-Nozzle Exhaust Flowfield," AIAA Paper 85-1193, 1985.

7. Lombard, C.K.: "Recent Development in the Upwind Implicit Method for the Compressible Navier-Stokes Equations," Presented as AIAA Paper 85-1659, 1985.
8. Yang, J.Y., Lombard, C.K. and Bardina, Jorge: "Implicit Upwind TVD Schemes for the Euler Equations with Bidiagonal Approximate Factorization," Presented at the International Symposium of Computational Fluid Dynamics, Tokyo, Japan, 1985.
9. Venkatapathy, E., Palmer, G., Deiwert, G.S. and Lombard, C.K.: "An Efficient Adaptive Patched Grid Gas Dynamic Solver for Complex Flows," AIAA-86-1288, 1986.
10. Lombard, C.K. and Venkatapathy, Ethiraj: "Implicit Boundary Treatment for Joined and Disjoint Patched Mesh Systems," Presented at the Nobeyama Workshop, Japan, 1985.
11. Berger, Marsha J. and Oliger, Joseph: "Adaptive Mesh Refinement for Hyperbolic Partial Differential Equations," *J. of Computational Physics*, Vol. 53, No. 3, March 1984, pp. 484-512.
12. Venkatapathy, Ethiraj and Lombard, C.K.: "Application of Patched Meshes to Viscous and Inviscid Flows," Presented at the Sixth GAMM Conference on Numerical Methods in Fluid Mechanics, Sept. 1985.
13. Goguen, J. A.: "Reusing and Interconnecting Software Components," *IEEE Computer*, pp. 16-28, Feb. 1986.
14. Chakravarthy, S.R. and Osher, Stanley: "A New Class of High Accuracy TVD Schemes for Hyperbolic Conservation Laws," AIAA Paper 85-0363, 1985.
15. Harten, A.: "High Resolution Schemes for Hyperbolic Conservation Laws," *J. Comp. Phys.*, Vol. 49, 1983, pp. 357-393.
16. Eriksson, Lars-Erik: "Three-Dimensional Spline-Generated Coordinate Transformations for Grids Around Wing-Body Configurations," *Numerical Grid Generation Techniques*, NASA CP 2166, 1980, pp. 253-264.
17. Eiseman, Peter R. and Smith, Robert E.: "Mesh Generation Using Algebraic Techniques," *Numerical Grid Generation Techniques*, NASA CP-2166, pp. 73-120, 1980.
18. Gordon, William J.: "An Operator Calculus for Surface and Volume Modeling," *Computer-Aided Geometry Modeling*, NASA CP 2272, 1983, pp. 1-5.
19. Baker, A.J. and Manhardt, P.D.: "Grid and Metric Generation of the Assembly of Locally Bi-Quadratic Coordinate Transformations," *Numerical Grid Generation Techniques*, NASA CP 2166, 1980, pp. 175-179.
20. Mitchell, A.R. and Wait, R.: *The Finite Element Method in PDE's*, John Wiley & Sons, NY, 1977.
21. Roe, P.L.: "The Use of the Riemann Problem in Finite-Difference Schemes," Seventh Internal Conference on Numerical Methods in Fluid Dynamics, *Lecture Notes in Physics*, 141, 1981, pp. 354-359.

## **2. Directed Graph Programming Environment**

Much, if not most, effort in science is devoted to communication between various media and processes. These links are man-machine, machine-machine, and program-program, etc. The purpose of this project is to develop an extensible framework in which this communication can efficiently take place and these processes controlled.

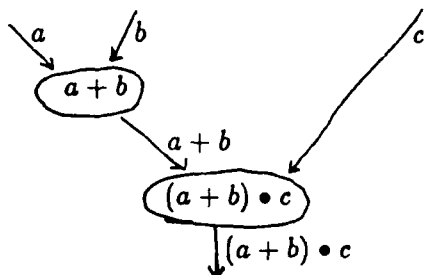
Man-machine interaction is especially costly and tedious when geometrically complicated problem domains need to be specified. The use of new architectures and algorithms or the introduction of new physics often pose severe time and cost penalties because of extensive software modifications. These two problems are being focused upon initially and the system will then be expanded in its role and functionality.

The system is envisioned to encompass:

1. Graphical input via a graph structured terminal interface
2. Graph structure top down/bottom up development system which facilitates combining existing code in different languages
3. An object oriented interprocess communication system with several levels of formality
4. Formal manipulation ability for derivations

### **Program Representation, Macrodataflow and Directed Graphics**

The major obstacle to building large programs from program fragments, and perhaps utilizing pre-existing programs, is the management of data and data structures. The program itself will have defined input and output and the program can be visualized as the process of performing a sequence of functions on the input in order to obtain the desired output. A program can be organized from the top down by specifying these functions and their relationship to one another. If the program is broken into rather large pieces called nodes involving several operations (functions) on several operands (data), then we can describe this process in terms of macro data flow. For each node we describe the data required for each functional operation, the functions to be performed, and the output to be produced. We then complete the specification of the program by linking these nodes together in the required order. This process can be described nicely using the idea of directed graphs. A directed graph consists of a collection of nodes  $N = \{n_i\}$  and links or edges  $E = \{e_{ij}\}$ . The edges  $e_{ij} = (i, j)$  are ordered pairs with tail  $i$  and head  $j$  leading from node  $n_i$  to node  $n_j$  and are unidirectional paths. The matrix  $E = \{e_{ij}\}$  made up of the array of edges is not generally symmetric. The nodes  $n_i$  can be used to define the processes and the edges used to describe the flow of data through the system. In a labeled directed graph labels  $l_i$  are attached to nodes to describe their function. On a very primitive level we can describe the computation of  $d = (a + b) \bullet c$  as



The first major step in the construction of a modern compiler is the construction of a directed graph which represents the computation. We plan to graphically describe the functions and their relationships to each other on a traditional subroutine or subprogram modularity. The graph then needs no artificial linear ordering. Its structure will be coupled with an abstract data description language which will provide a facility for the generation of filters. These filters will take output from existing programs and modify it for input to the succeeding node as required.<sup>1</sup>

#### Visual Graph Generating User Interface

We have well in development a visual communication system based upon windows and menus such as those used on the SUN workstations. We intend to extend this capability by implementing a hierarchy of menus in a tree structure. In the program development environment the relationships of processes are explicitly defined by connecting windows to one another via a directed graph which then serves as the (executable) program control. No linear program is required and this organization can be done differently for different hardware systems to take advantage of parallel or vector processing, etc. The basic operations are the construction of a graph via windowing software, the "execution" or traversal of such a graph, and the graphical display of the graph for the user during definition and modification. This is an object oriented system with automatic compatibility of domains and ranges, etc. Each "window" may contain subwindows or programs in different languages, initially at least FORTRAN, PASCAL and C.

#### Interprocess Communication

Communication between logical sections of programs (windows) will be object oriented and file based. However, several levels of formality will be available. An informal level like that afforded by UNIX pipes will be followed by more formal files with internally defined structures and features which allow traces, etc. Finally, formal communication with a permanent database will be implemented and be message based. Our implementation will be a macro dataflow system without interprocess side effects.

Our more formal files with internally defined structures will be used to communicate and translate data between formats and/or data structures to allow the interaction of programs. This allows us to provide an upward extensible but downward compatible environment when we enable processes to read files extracting only those segments that they "understand".

## Implementation

We plan to implement this system in the spirit in which it is planned to operate - it will be built up using as much available software as possible. Pieces will be redesigned only when it becomes obvious that it is desirable to do so.

Our system will be UNIX based and interact with programs at the operating system level, i.e., we will execute our graphics, not merely concatenate them as files, etc. We plan to use windowing features and existing workstations and software to build from.

In particular, we plan to incorporate the MACSYMA Symbolic manipulation system or equivalent. We are currently searching existing software for graphics and designs and evaluating which would incorporate best.

## References

1. A. Aho, J. Hopcroft, J. Ullman: *Data Structures and Algorithms*, Addison-Wesley, Reading, Mass., 1983.

### **3. Accurate Numerical Simulation of Supersonic Jet Exhaust Flow with CSCM on Adaptive Overlapping Grids**

Design of propulsive systems, drag reduction and stability in re-entry vehicles, projectiles, missiles and other supersonic aerodynamic bodies require design and analysis computational tools that can accurately predict the overall flow and in particular the base flow. The numerous numerical schemes available today have their own virtues and limitations. The present paper outlines and applies the coupled overlapping grids CSCM scheme<sup>1,2,3,4</sup> and self-adaptive grid scheme<sup>5,6</sup> to the jet exhaust base flow problem. The work culminates a series<sup>4,7</sup> of numerical experiments in the effects of mesh topology and resolution on base flow prediction. All the computational experiments have been made with the same adaptation<sup>7</sup> of the Baldwin-Lomax<sup>8</sup> algebraic eddy viscosity model of turbulent interaction. Here computed adaptive grid solutions are presented and comparisons with results of experiment and other numerical schemes are made. Great improvement to the flow solutions are achieved through flow structure adaptive regridding and the computed base pressure distribution compares very well with experimental predictions of Petrie and Walker<sup>9</sup>.

In recent years evolving computational techniques have been used to predict supersonic viscous base flows<sup>4,5,7-23</sup> in a variety of situations. Complexity of the supersonic base flow features and the topological difficulty of the flow region have led to discretization of the flow field in different ways<sup>4,7,9,11,15,17,19,23</sup>. Most numerical schemes through their programming have been limited to obtaining solution in a single rectangular computational domain. Hence the base flow region is often discretized by a wraparound grid or with rectangular composite block grids. Recent advances in data structure and boundary treatment have opened the way to novel grid techniques<sup>1,2,3,4</sup>, such as multiple patched and overlapping grids, and have provided alternatives to solving the flow field in simple rectangular computational domains. Finally, the use of auto-adaptive grid procedures results in appropriate grid point redistribution and improves solution accuracy greatly with minimal computer and human effort. The resulting improvement in local flow structure capture in turn improves the overall solution accuracy.

#### The Tactical Missile Turbulent Base Flow Problem

A cold flow model tactical missile turbulent base flow was experimentally studied at AEDC and the experimental results and other numerical predictions were reported in Ref. 9. The axisymmetric flow experiment featured a tangent ogive-cone-cylinder body terminating in a square base. The propulsive jet flow exhausted into the base region through a centered transonic nozzle with a flush exit. The nozzle occupied 0.2 diameter at the exit plane and the model was 9 diameters long. The free stream Mach number was maintained at 1.4 and the Reynolds number of the flow based on base diameter was  $0.92 \times 10^6$ . The nozzle jet flow at the exit was at a nominal Mach number of 2.7 and the nozzle exit pressure ratio was 2.15 relative to the free stream pressure. Other relevant wind tunnel conditions are given in Ref. 7.

The schematic of the above flow is shown in Figure 1. The supersonic external flow and the nozzle exhaust flow both undergo strong expansions around the corner regions followed by recompression. The flow separation in the base region requires the flow to turn with a recompression shock near the outer flow region and a barrel shock near the axis being formed. In addition, strong shear layers and associated counter rotating vortices form in the base region. Mach disk and reflected shocks also occur within the flow domain. The occurrence and interaction of the above mentioned flow features make the jet exhaust base flow problem very interesting but difficult to compute. As is well known, accurate base pressure prediction has been very difficult to achieve. The prediction depends very much on the appropriateness of the grids and the accuracy of the boundary and interior difference schemes. The present study indicates that an algebraic model of turbulence<sup>7</sup> with roughly appropriate length scale and velocity measures can perform, perhaps surprisingly, well.

### Computational Approach

Numerical solutions to the base flow problem have been obtained using various schemes and Ref. 16 reviews most results. Solutions to the base flow problem using the Conservative Supra Characteristic Method<sup>24</sup> (CSCM) with a wraparound and a simple Cartesian step grid are presented in Ref. 7. As pointed out there, it is not possible to achieve adequately balanced resolution with simple mesh topologies on geometrically complex flow domains.

Overlapping grids are natural and appropriate for complex flows. The choice of locally topologically appropriate, multiple, independent overlapping grids alleviates the geometric difficulty<sup>3,4</sup>. With well balanced resolution, the resulting global solution is more accurate. The use of multiple grids simplifies the discretization of the complex physical domain and allows the easy use of a solution adaptive scheme. Corner regions are modelled accurately with appropriate local wraparound grids.

The details of the CSCM scheme for multiple overlapping grids and the interior grid boundary data procedure are given in Ref. 1 and 2. The overlapping grid CSCM data structure takes proper care of information transfer between grids. The stable characteristics based boundary data transfer procedure and the interior upwind difference scheme together predict smooth solution everywhere. Shocks and other discontinuities pass from one grid to the other without distortion. Solutions to complex shock reflection problems with overlapping grids were reported in Ref. 2 and 4.

Once a converged solution is obtained on the initial grids, the self adaptive grid scheme of Nakahashi and Deiwert<sup>5</sup> is applied and the grid points are moved in all the grids according to the specified constraints and flow variations. The adaptive gridding is done in all coordinate directions. Then starting with the interpolated solution on the adapted grid, converged solutions are obtained using the CSCM procedure once again. Further grid adaptations and computation cycles are done if necessary but not employed for the results presented here.

### Results and Discussion

Seven overlapping grids are used in the present problem. The first grid covers the transonic nozzle and the second grid extends from the first grid down towards the outflow boundary and covers the exhaust jet. The third grid is used for the outer flow up to the base and the fourth grid, similar to the second grid, extends from the third grid downstream to the outflow. The fifth grid covers the base flow region. The sixth and seventh grids are local wraparound corner grids at the lower and upper base corner regions. Figure 2 shows the boundaries of each grid and Figure 3 shows the overlapping grids. All the grids have at least two cell overlap with their neighbors. The grid points in grids 1, 3, and 5 are clustered to the wall to resolve the viscous layer. A blow up of the grids near the nozzle exit plane, given in Figure 4, shows the grid structure in the vicinity of the corner. Each of the seven grids span a much simpler sub-region of the global physical domain. All grids were generated using an interactive algebraic grid generation scheme<sup>25</sup>. We note that with the technique, since each sub-grid spans only a simpler region, it would be very easy to implement nozzle or external design (shape) changes without changing the grid globally.

The interface boundary conditions for the upwind schemes have been solved satisfactorily and are addressed in Ref. 1. In this paper we apply the characteristic interpolated boundary treatment<sup>1</sup> at all overlapping interior boundaries and appropriate physical boundary conditions<sup>24,26</sup> are applied at the boundaries of the computational domain. At all the wall boundaries adiabatic, no slip boundary conditions are imposed.

The flow is nearly stagnant at the inflow to the nozzle section with a stagnation pressure of 307.7 psi and stagnation temperature of 207.0° F. Experimentally measured flow conditions<sup>18</sup> are imposed along the inflow boundary of grid 3, at a station 16 nozzle exit radii upstream of the base. The outer flow Mach number is 1.343. With these specified conditions a converged steady state solution is obtained using the CSCM method. In the nozzle and in the outer supersonic regions, thin layer Navier-Stokes equations are solved. In the base flow region, (grid 5) viscous stresses along both computational coordinate directions are included. An algebraic turbulent eddy-viscosity model<sup>8</sup> reported in Ref. 7 is adapted here to model the turbulent interaction. In grids 1, 3, 6 and 7 wall turbulence model is used and in grids 2, 4 and 5 a wake model is used. A solution of spatially second order accuracy is obtained in about 600 iterations. Mach contours of the computed solution without mesh adaptation are shown in Figure 5. The contour plots show the strong expansion regions, the recompression shock, the barrel shock, the mach disk, the reflected shock and the shear layers.

### Solution Improvement with Adaptive Grids

Further improvements to the above solution without the addition of more grid points is easily achieved with the self-adaptive grid technique of Nakahashi and Deiwert<sup>5</sup>. The adaptive grid scheme is automatic, simple to use and very flexible. Grids can be adapted in all coordinate directions and grid adaptation can be performed globally or locally.

The self-adaptive grid technique has been used in the past with simple and block grids. The redistribution of grid points in the overlapping grids is more involved, but not

too difficult depending on the choice of the overlapping grids. With adaptive regridding, some of the interior patch boundaries (that do not conform to physical boundaries) should deform according to the flow features, but physical boundaries such as wall, inflow, axis and outflow boundaries should remain fixed. With present programming, if each grid is adapted independently, then all the interior boundaries will remain fixed. To allow the interior boundaries to move, a block of grid points in the region of interest are assembled from all the grids and these grid points are moved according to the constraints specified. After regridding, a reverse transformation which preserves the original overlap is performed and individual, overlapped, adapted grids are formed. This procedure does not alter the basic auto-adaptive grid code or the flow solver.

Based on the converged solution shown in Figure 5, the grids after many global and local adaptations from the grids of Figure 3 appear as shown in Figure 6. The adapted grids show all the prominent features of the flow field (Figure 5) based on which the adaptation was performed. A combination of Mach number and density variations were used in developing the adapted grids. Since the adaptation is a result of flow variation and user specified constraints, care must be taken during adaptation. It is possible to over-adapt. A rule of thumb is to first adapt globally and then adapt locally to flow structures.

Steady, converged solution on the adapted grid is obtained in another 200 steps. Interpolated solution from the non-adapted grid served as the starting solution. The converged adaptive grid solutions are presented in terms of pressure, density, Mach and temperature contours in Figures 7 through 10. Comparing Figures 5 and 9, one can see that the adapted grids indeed serve to capture the flow better and the flow structure details are more prominent than on the non-adapted grid solution. Specially the shear layer features and the Mach disc and the reflected shock near the axis are captured more sharply. The merging of the shear layers is best seen from the temperature contour plots. Complex flow interactions between the shear layers, and the recompression and barrel shocks determine the size and shapes of the separated base flow near the annular base region. The predicted base pressure profiles with and without grid adaptation are compared with the experimentally measured pressures in Figure 11. Base pressure predictions from other numerical results taken from Refs. 4 and 9 are reproduced here in Figure 12. The adapted overlapping grids solution predicts base pressure significantly better compared with non-adapted solution and other numerical predictions. As is well known and reinforced by the present results, the base pressure is very sensitive to the flow details in the base regions. It is our belief that the adapted grids, particularly through accurate capture of the shear layers, allows the flow field near the base region to evolve accurately and this coupled with proper application of the adiabatic boundary conditions at the base wall recovers the correct base pressure. In Figure 13, the velocity vectors are shown. Various recirculating vortices are clearly visible. In Figure 14, stream lines as particle traces are shown. The particles are released all along the exit plane and the resulting particle traces give further insight into the physical aspect of the flow. The particle released from the top half of the annular regions is lifted up, and turns downward and reaches the nozzle exit corner. From there they are convected downstream through various vortices. The empty regions, representing

the stagnant regions show the location of slower moving vortices region. The Mach number profile along the axis from the non-adapted and adapted solutions are shown in Figure 15. The Mach number is a little higher than 1.0 behind the shock reflection point (where it should be 1.0) Through further local refinement and adaptation, the Mach disc can be captured better.

#### Concluding Remarks

The self-adaptive grid scheme of Nakahashi and Deiwert coupled to the overlapping grids CSCM scheme is demonstrated to be very effective in obtaining accurate solutions to the complex jet exhaust base flow problem. The adapted overlapping grid solution captures all the important flow features accurately and the flow details agree very well with experimental observation. Further, excellent agreement between the predicted base pressure and the experimental results increases the confidence in present flow solver and grid strategy. The flexibility of the combined adaptive and overlapping grids makes the CSCM flow solver a very effective design and analysis tool.

#### References

1. Lombard, C.K. and Venkatapathy, Ethiraj: "Implicit Boundary Treatment for Joined and Disjoint Patched Mesh Systems," AIAA-85-1503, 1985.
2. Venkatapathy, Ethiraj, and Lombard, C.K.: "Flow Structure Capturing on Overset Patched Meshes," AIAA-85-1690, 1985.
3. Venkatapathy, Ethiraj, and Lombard, C.K.: "Application of Patched Meshes to Viscous and Inviscid Flows," *Proceedings of the Sixth GAMM-Conference on Numerical Methods in Fluid Mechanics*, Eds. D. Rues and W. Kordulla, Friedr. Vieweg and Sohn, 1986.
4. C. K. Lombard, J. Bardina, E. Venkatapathy, J. Y. Yang, R. C. C. Luh, N. Nagaraj, and F. Raiszadeh: "Accurate, Efficient and Productive Methodology For Solving Turbulent Viscous Flows in Complex Geometry" presented at the Tenth International Conference on Numerical Methods in Fluid Dynamics, Beijing, China, June, 1986.
5. Nakahashi, K. and Deiwert, G. S.: "A Self-Adaptive-Grid Method with Applications to Airfoil Flows", AIAA-85-1525, 1985.
6. Venkatapathy, Ethiraj, G. Palmer, G. S. Deiwert and C. K. Lombard: "An Efficient Adaptive Patched Grid Gas Dynamic Solver for Complex Flows," AIAA-86-1288, 1986.
7. C. K. Lombard, R. C. C. Luh, N. Nagaraj, J. Bardina and E. Venkatapathy: "Numerical Simulation of Backward Step and Jet Exhaust Flows," AIAA-86-0432, 1986.
8. Baldwin, B.S. and Lomax, H.: "Thin Layer Approximation and Algebraic Model for Separated Turbulent Flows," AIAA-73-0257, 1973.
9. Petrie, H.L. and Walker, B.J.: "Comparison of Experiment and Computation for a Missile Base Region Flowfield with a Centered Propulsive Jet," AIAA-85-1618, 1985.
10. Deiwert, G.S.: "A Computational Investigation of Supersonic Axisymmetric Flow Over Boattails Containing a Centered Propulsive Jet," AIAA-83-0462, 1983.

11. Sahu, J., Nietubicz, C.J. and Steger, J.L.: "Navier-Stokes Computations of Projectile Base Flow with and without Base Injection," AIAA-83-0224, 1983.
12. Putnam, L.E. and Hodges, J.: "Assessment of NASA and RAE Viscous-Inviscid Interaction Methods for Predicting Transonic Flow Over Nozzle Afterbodies," AIAA-83-1789, 1983.
13. Lombard, C.K., Bardina, J. and Venkatapathy, E.: "AOTV Bluff Body Flow - Relaxation Algorithm," in *Thermal Design of Aeroassisted Orbital Transfer Vehicles*, Ed. H. F. Nelson, Progress in Astronautics and Aeronautics, Vol. 96, 1985, pp. 85-112.
14. Reklis, R.P. and Conti, R.J.: "Computational Probing of Hypersonic Laminar Wakes," AIAA-84-1579, 1984.
15. Luh, Raymond C.-C. and Lombard, C.K.: "Projectile Aerodynamics Prediction with CSCM-S Upwind Implicit Relaxation Algorithm," AIAA-85-1838, 1985.
16. Scott, J.N. and Hankey, W.L., Jr.: "Numerical Simulation of Cold Flow in an Axisymmetric Centerbody Combustor," AIAA-83-1741, 1983.
17. Bardina, Jorge and Lombard, C.K.: "Three Dimensional CSCM Method for the Compressible Navier-Stokes Equations with Application to a Multi-Nozzle Exhaust Flowfield," AIAA-85-1193, 1985.
18. Putnam, L.E. and Bissinger, N.C.: "Results of AGARD Assessment of Prediction Capabilities for Nozzle Afterbody Flows," AIAA-85-1464, 1985.
19. Deiwert, G.S., Andrews, A.E. and Nakahashi, K.: "Theoretical Analysis of Aircraft Afterbody Flow," AIAA-84-1524, 1984.
20. Wagner, B.: "Calculation of Turbulent Flow About Missile Afterbodies Containing an Exhaust Jet," AIAA-84-1659, 1984.
21. Sahu, J.: "Computations of Supersonic Flow Over a Missile Afterbody Containing an Exhaust Jet," AIAA-85-1815, 1985.
22. Sahu, J. and Nietubicz, C.J.: "Numerical Computation of Base Flow for a Missile in the Presence of a Centered Jet," AIAA-84-0527, 1984.
23. Thomas, P.D., Reklis, R.P., Roloff, R.R. and Conti, R.J.: "Numerical Simulation of Axisymmetric Base Flow on Tactical Missiles with Propulsive Jet," AIAA-84-1658, 1984.
24. Lombard, C.K., Bardina, J., Venkatapathy, E. and Oliker, J.: "Multi-Dimensional Formulation of CSCM - An Upwind Flux Difference Eigenvector Split Method for the Compressible Navier-Stokes Equations," AIAA-83-1895, 1983.
25. Luh, R. C-C., Nagaraj, N., and Lombard, C. K.: "Algebraic Grid Generation," AIAA 87-0200, January 1987.
26. Lombard, C.K., Bardina, Jorge and Luh, Raymond Ching-Chung: "Implicit Numerical Boundary Procedures Applied in the CSCM Upwind Algorithm with Characteristic and Characteristic-Like Extrapolations," to be presented at the Numerical Methods in Laminar and Turbulent Flow Conference in Montreal, Canada, July, 1987.

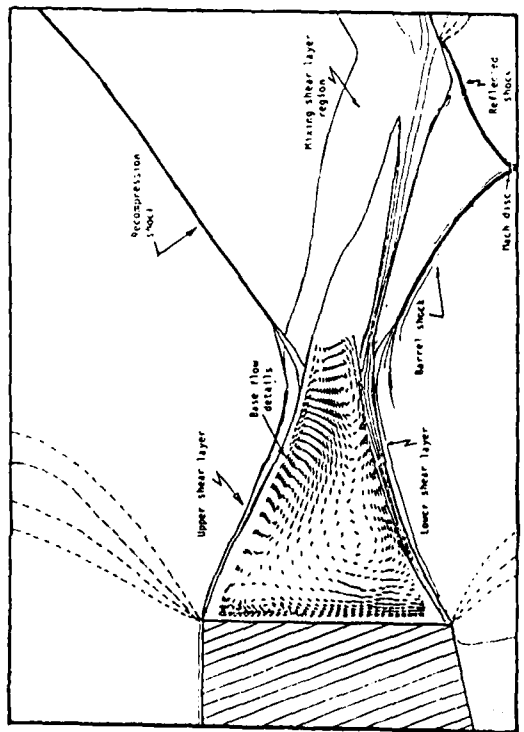


Figure 1. Schematic of the jet exhaust base flow.

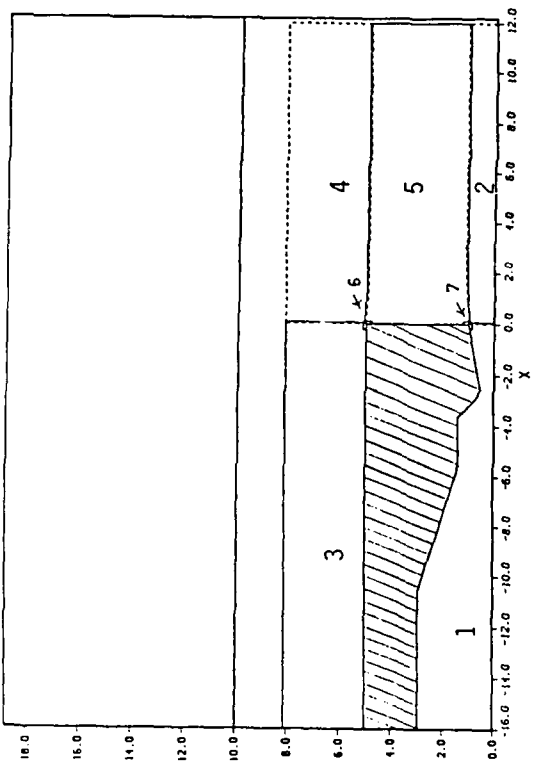


Figure 2. Overlapping grid boundaries.

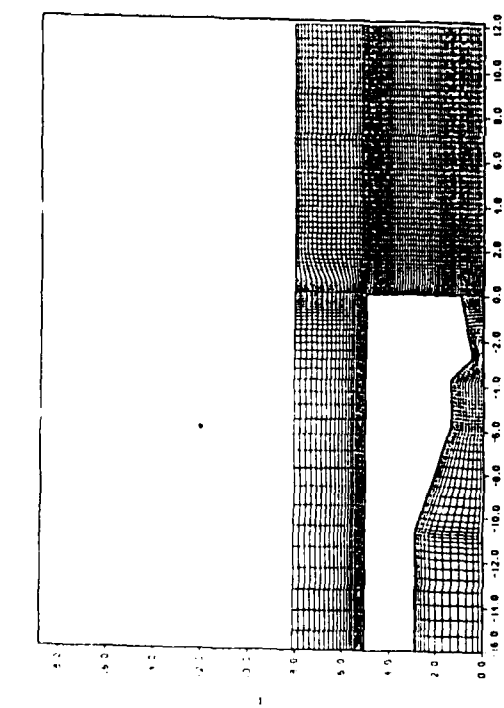


Figure 3. Overlapping grids for the complete base flow.

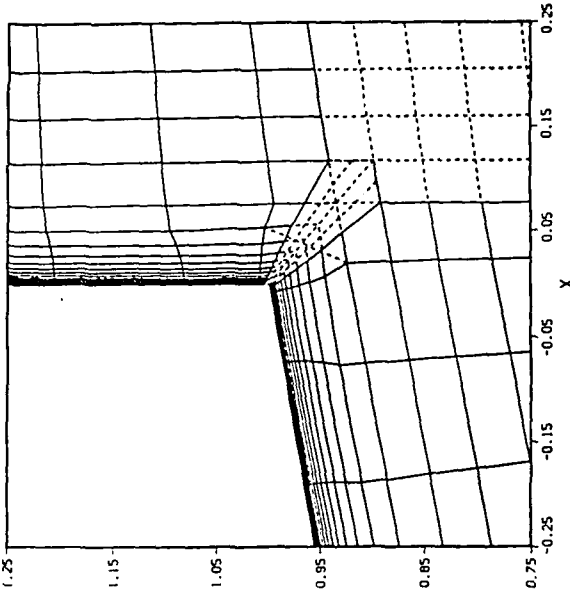


Figure 4. Grids in the vicinity of a corner.

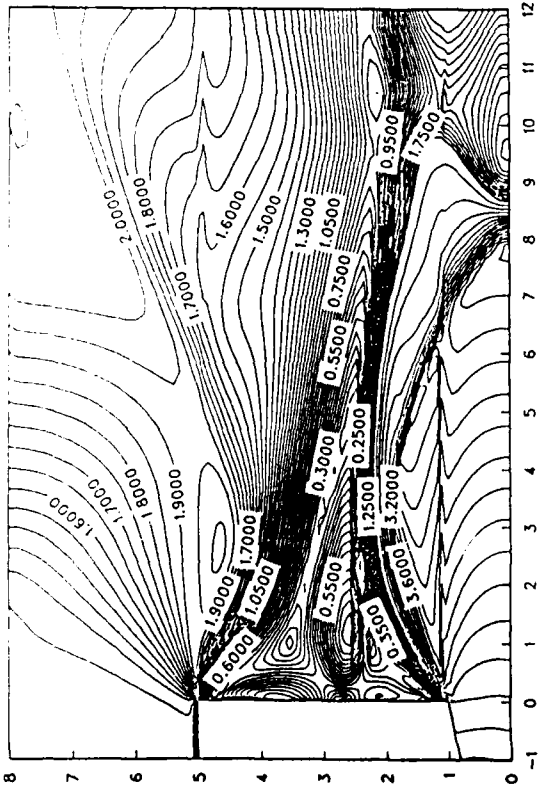


Figure 5. Mach contours — second order overlapping, nonadapted grids solution.

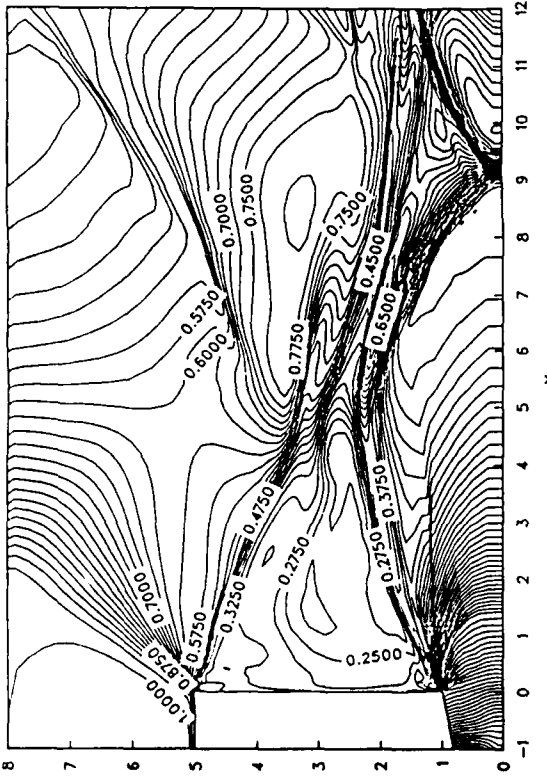


Figure 7. Density contours from the adapted grids solution.

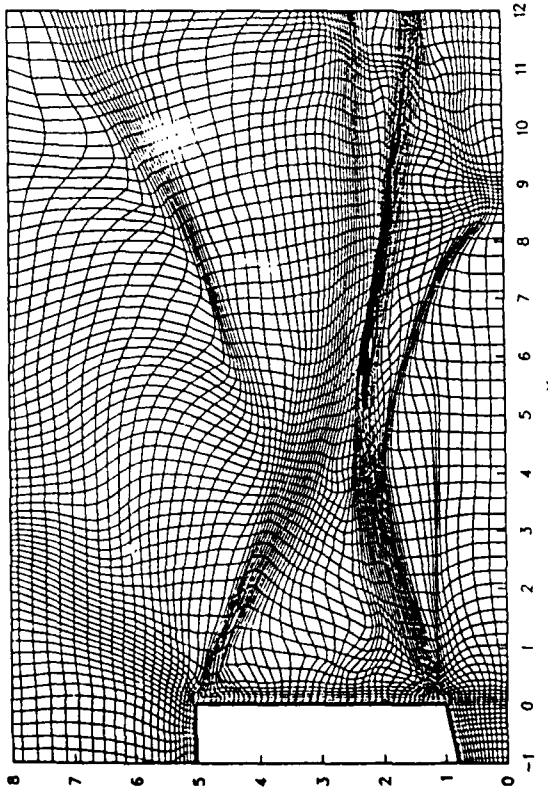


Figure 6. Adapted overlapping grids.

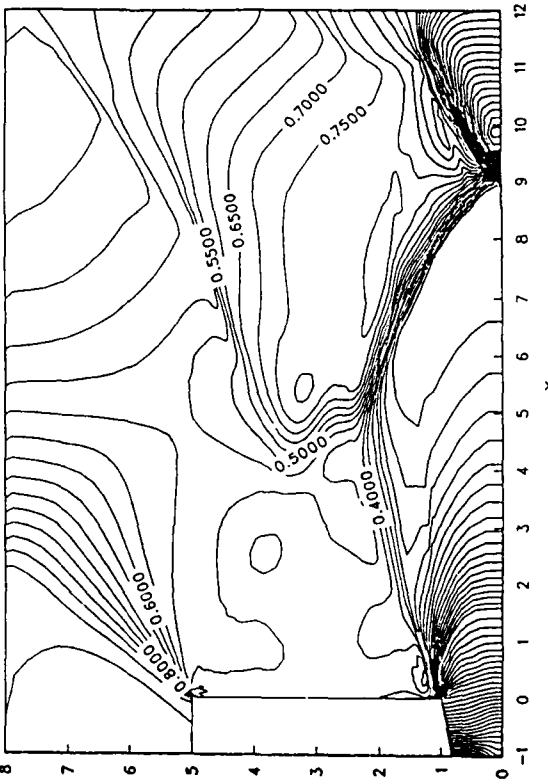


Figure 8. Pressure contours from the adapted grids solution.

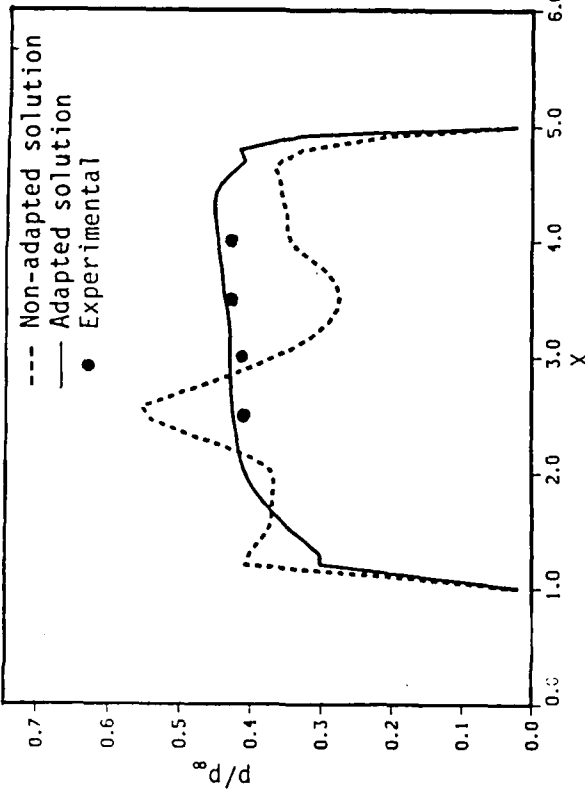


Figure 11. Base pressure comparison.

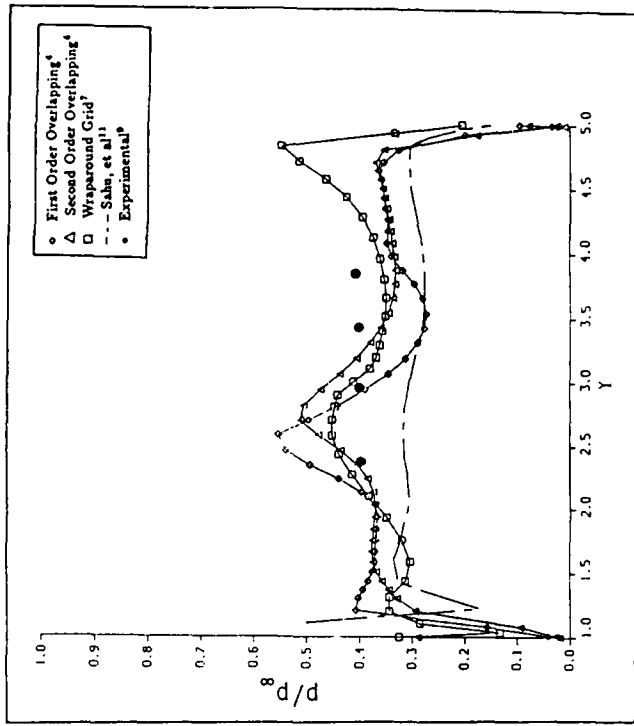


Figure 12. Base pressure prediction (Refs. 4 and 9).

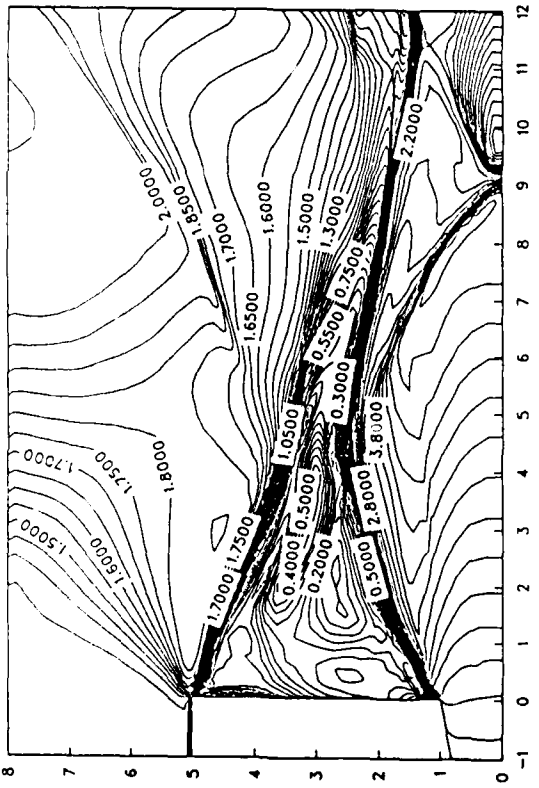


Figure 9. Mach contours from the adapted grids solution.

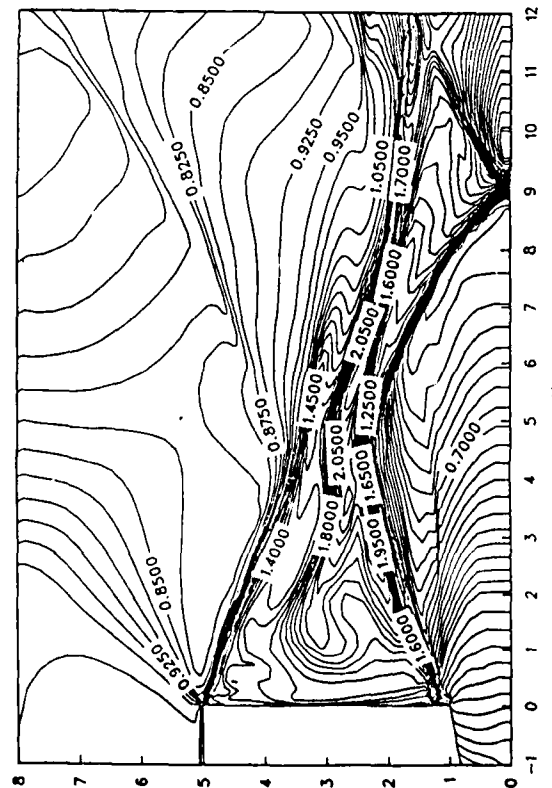


Figure 10. Temperature contours from the adapted grids solution.

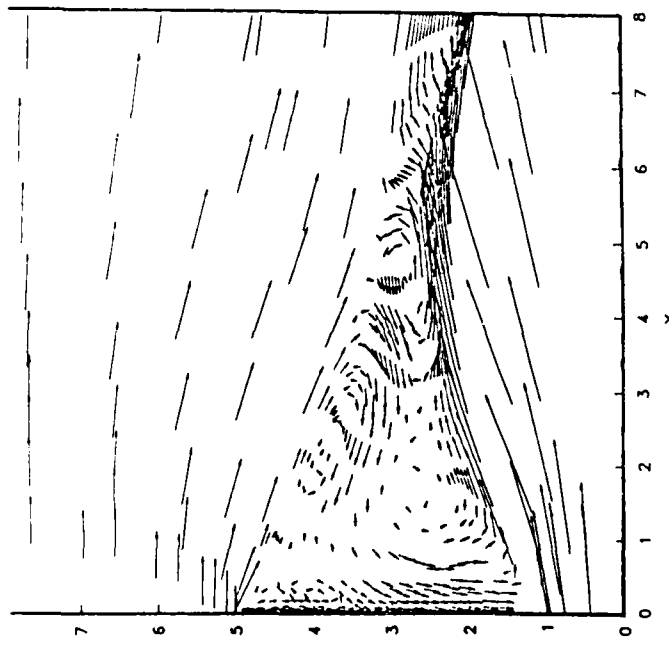


Figure 13. Velocity vectors in the base region.

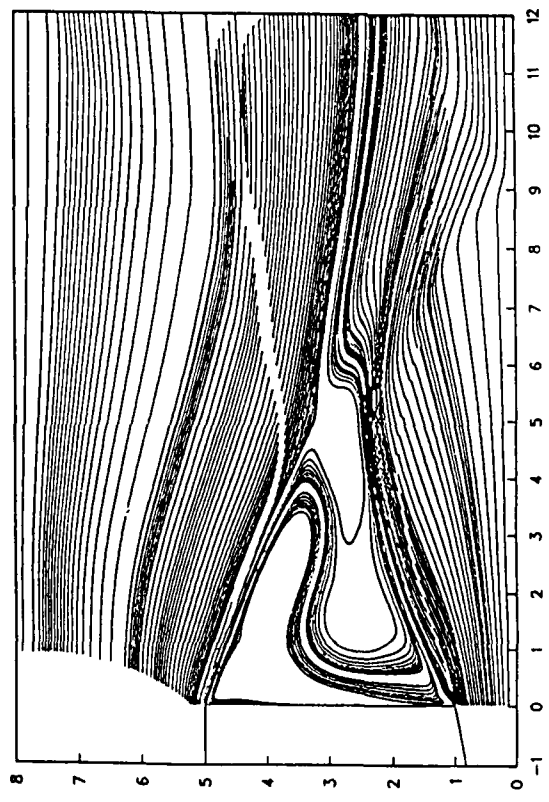


Figure 14. Stream lines in the base region.

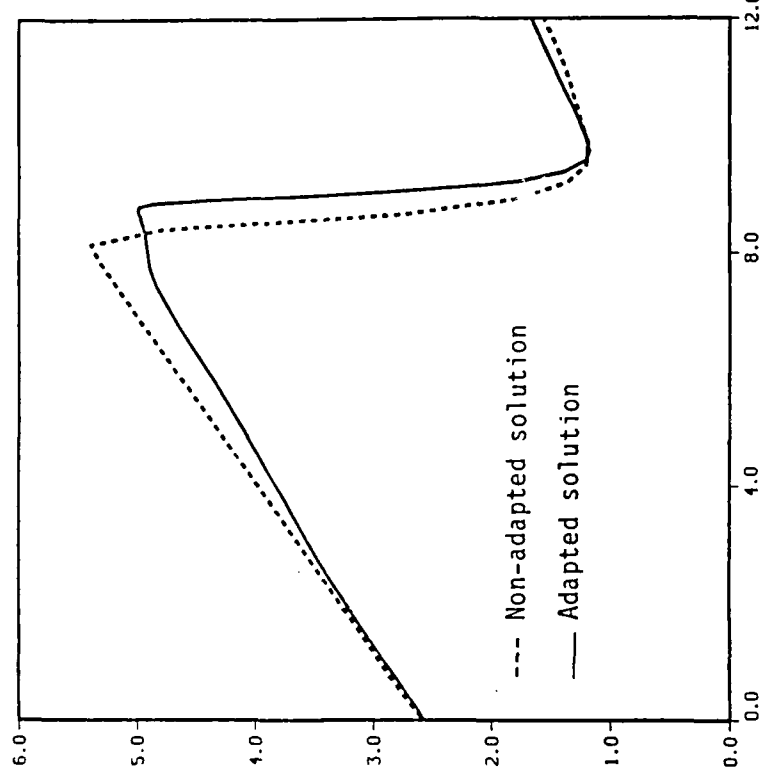


Figure 15. Mach number along the axis.

#### 4. Accurate, Staggard Grid Upwind Schemes on Biased Upwind Cells

If one sees the seventies and first half of the eighties as a period of learning how to construct stable, accurate and computationally fast methods to solve compressible flow equations, particularly the Navier-Stokes equations, then it is quite apparent the focus is shifting and for a time the emphasis will be on synthesis, application and enhanced productivity. The present paper introduces improvements in the multi-dimensional formulation, numerical implementation and mode of application of the implicit Conservative Supra-Characteristics Method (CSCM). The method for both the compressible Euler and Navier-Stokes equations was first presented for inviscid quasi one dimensional flow in the 8th ICNMF by Lombard, Oliker and Yang<sup>1</sup>. Extension of CSCM to a 2-D and source term free axisymmetric formulation was given by Lombard, Bardina, Venkatapathy and Oliker<sup>2</sup>. Reference 2 introduced solution of the difference equations by a two data level block tridiagonal procedure based on a diagonally dominant approximate factorization DDADI. Subsequent extensions of that approximate factorization were shown by Lombard, Venkatapathy and Bardina<sup>3</sup> to form the basis for a family of single data level operationally explicit implicit relaxation algorithms. One of those algorithms, a symmetric Gauss-Seidel space marching procedure implemented as a method of lines in two space dimensions (or planes<sup>4</sup> in three dimensions) was found to be an order of magnitude more rapidly convergent to steady state than the same equations solved in the two level linearized pseudo time relaxation procedure. In the generalized Roe form<sup>5</sup>

$$\tilde{A} \Delta q \equiv \Delta \tilde{F} \quad (1)$$

which relation is preserved by the CSCM constructed matrix, the adjacent grid point interval averaged Jacobian matrix  $\tilde{A}$  onto the conservative variable difference is used to represent the flux difference. Thus updating  $\tilde{A}$  and  $q$  in the locally iterated pseudo time relaxation procedure at each marching step is equivalent to updating the flux.

Heretofore we wrote<sup>3</sup> the method (here sketched as a first order single level method in one dimension) as

$$D \delta q = -\tilde{A}^+ \nabla q - \tilde{A}^- \Delta q \quad (2)$$

where  $D = J/\Delta t(I + \tilde{A}^+ - \tilde{A}^-)$  with  $J$  a measure of computational cell volume and  $\tilde{A}^\pm$  are the eigenvector split pieces of the Jacobian matrix according to

$$\tilde{A}^\pm = (\bar{M} \bar{T} I^\pm \bar{T}^{-1} \bar{M}^{-1}) \tilde{A} \equiv \hat{A}^\pm \tilde{A} \quad (3)$$

with  $I^\pm = \frac{1}{2}(I \pm \text{sgn}\bar{\Lambda})$ . Thus as shown in reference 1,

$$\tilde{A}^\pm \Delta q \equiv \hat{A}^\pm \Delta \tilde{F} = \Delta \tilde{F}^\pm . \quad (4)$$

### Flux Divergence Upwind Methods

To begin the present developments, we now write the equivalent

$$D \delta q = -\nabla \tilde{F}^+ - \Delta \tilde{F}^- = -\hat{A}^+ \nabla \tilde{F} - \hat{A}^- \Delta \tilde{F}. \quad (5)$$

In two or more space dimensions flux difference terms such as appear on the right hand side of equation (3) for each coordinate direction can be written either in strong or chain rule (Hindman<sup>6</sup>) conservation law forms according as the metric coefficients of the differential transformation

$$\partial \tilde{F} = \xi_x \partial F + \xi_y \partial G \quad (6)$$

are represented under or outside of the difference approximations. In the latter case, averaging the metric coefficients on the difference interval is appropriate for Roe form schemes. While in quasi one dimensional flow the upwind method<sup>1</sup> with strongly conservative differencing was found to be very robust and accurate, in 2-D or axisymmetric flow the chain rule approach<sup>2</sup> was found to work far more reliably. We will explain why we believe this is so and present alternative strong conservation law formulations that according to the rationale are both stable and more accurate than chain rule. In the process we will show how to overcome a problem associated with nonorthogonal grids.

### Chain Rule Conservation

The chain rule conservation law form for discrete differences is the natural approximation to equation (6). For central difference methods in strong conservation law form, it has long been recognized and practiced<sup>6,7,8</sup> that the numerical divergence of the metric coefficients must be zero under the operations of the finite difference method in order for the method to meet the minimal requirement to preserve a uniform flow. However in upwind methods, particularly those in generalized Roe forms, this fact has been to a greater or lesser extent ignored and stability appealed to based on global conservation of the telescoping difference equations. The problem we will cite also exists for some higher order upwind methods with a numerical flux function in the node centered classical finite volume cell format and when using non cell face local metric coefficients.

The issues associated with local conservation, which we espouse here, can be seen simply geometrically. In Figure 1, we show the computational cell associated with one sided differencing for the  $\xi$  direction. For what we may term local geometric conservation in the cell, we consider the flux vector component  $\tilde{F}_\xi$  for the  $\xi$  direction. The flux tensor has two components  $\tilde{F}_\xi$  and  $\tilde{F}_\eta$ . For the moment, the other component of the flux tensor will be regarded as treated in another ( $\eta$ ) family of cells aligned with the  $\eta$  coordinate direction. The flux vector must be projected not only through the end faces  $i$  and  $i + 1$  in the  $\xi$  direction but also through the lateral side faces  $k \pm \frac{1}{2}$ . The associated difference relation is symbolized

$$\Delta \bullet \tilde{F}_\xi \equiv \Delta_\xi \hat{\xi} \bullet \tilde{F}_\xi + \delta_\eta \hat{\eta} \bullet \tilde{F}_\xi \quad (7)$$

Simple globally conservative one sided differencing ignores the second term of the right hand side of relation (7) and, as a consequence, introduces spurious numerical sources and sinks<sup>9</sup> that compromise accuracy and stability.

It is illuminating and easy to show that if the flux components  $\tilde{F}_\xi$  for the lateral  $\eta$  faces of the cell are approximated local to the cell by  $\tilde{F}_\xi|_{k \pm \frac{1}{2}} = \frac{1}{2}(F_\xi|_i + F_\xi|_{i+1})_k \equiv \bar{\tilde{F}}_\xi$  relation (7) is identically equivalent to chain rule differencing  $\hat{\xi} \bullet \Delta_\xi \tilde{F}_\xi \equiv \Delta \bullet \tilde{F}_\xi - \bar{\tilde{F}}_\xi \Delta_\xi \bullet \hat{S}$ . Here we assume the cell is properly closed and the metrics satisfy  $\Delta_\xi \bullet \hat{S} = 0$ .

Accordingly, the consequence of applying the chain rule conservation form is that in the laterally adjacent cells the similar flux approximations at  $k \pm 1$  through the shared faces  $\hat{\eta} \pm \frac{1}{2}$  are inconsistent with the approximation for cell  $k$  and the method is in general neither locally nor globally conservative. Two exceptions to the conclusion are found in the cases of uniform flow, which the chain rule method preserves, and no flow through the lateral sides as in the quasi 1-D stream tube approximation for which we had very good success<sup>1</sup> in strongly conservative differencing. Thus in principle the chain rule and simple globally conservative locally one dimensional methods are relatively more effective where the grid is nicely flow aligned, smooth gradients are weak and discontinuities are orthonormal. In practice chain rule conservation, with similar one sided difference terms for the  $\eta$  coordinate direction, works quite well<sup>2,3</sup> for the numerically dissipative first order method. For second order methods with limiters the error in conservation is diminished but the methods also decline in robustness, about which more will be said later.

#### Locally One Dimensional Strong Conservation

The conclusion from the above discussion is that a method closely akin to the chain rule locally one dimensional one sided upwind differencing procedures of references 2, 3 and 10 but which features consistent local geometric conservation for each flux component in its own family of one sided cells is obtained by replacing the simple one sided flux difference  $\Delta_\xi \tilde{F}_\xi$  for equation (5) by cell flux divergences symbolized by  $\Delta_\xi \bullet \tilde{F}_\xi$  with the lateral  $\hat{\eta}$  side fluxes in equation (7) given a symmetric definition, for example averaged between  $k$  and  $k+1$ . Similar generalized one sided upwind difference expressions are given for the  $\eta$  coordinate direction and we can write

$$D\delta q = -\tilde{A}_\xi^+ \nabla_\xi \bullet \tilde{F}_\xi - \hat{A}_\xi^- \Delta_\xi \bullet \tilde{F}_\xi - \hat{A}_\eta^+ \nabla_\eta \bullet \tilde{F}_\eta - \hat{A}_\eta^- \Delta_\eta \bullet \tilde{F}_\eta \quad (8)$$

This approach is both globally conservative and more consistent with the accuracy aims of local conservation and accordingly is expected to be more stable and robust. The above locally one dimensional approach has a numerical virtue in that the splitting operators apply homogeneously and rationally to their own convective fluxes.

There are, however, drawbacks still to be addressed. The first of these deals with nonorthogonal meshes. While the problem is not observed numerically to be severe for moderate deviations from orthogonality, from equation (8) it is obvious that in the limit as the mesh is skewed and the  $\eta$  and  $\xi$  fluxes become identical, other effects aside, the

method loses information from one sector of the flow domain and its solution must become inconsistent with the multi-dimensional PDE. A second weakness is that for general curvilinear coordinates the  $\xi$  direction in the Cartesian bases changes from cell to cell so there is not a unique and consistent direction on which to effect the flux decomposition and satisfy assumptions. A third weakness is that in the locally one dimensional method neither the partial nor total flux is identically conserved locally in each family of cells. The significance is that residual reduction at convergence may not be as firm as with the last method.

#### Symmetric Locally One Dimensional Conservation

Objections one and two above may be overcome by constructing methods that are symmetric overall in the two families of cells. By this we mean that all the cells of the procedure are shared among the two coordinate directions; a  $\xi$  one sided difference cell for one coordinate is also an  $\eta$  cell for the other coordinate. A last requirement for symmetry is that a unique definition of total flux be given for every cell face. These conditions ensure that regardless of the bases for flux tensor decomposition in adjacent cells, the total flux that numerically flows out of a face of one cell also flows through the same face into its neighbor cell.

Beyond the classical node centered finite volume, two kinds of computational cells can lend themselves to the construction of symmetric strongly conservative biased upwind methods. One of these cell types is the natural mesh cell bounded at the four corners (in 2-D) by its data nodes. The other is the laterally symmetric and upwind (coordinate) biased cell of Figure 1.

#### Symmetric Methods in Natural Mesh Cells

Of two approaches we have considered, one splits the weighted average of the flux divergences in adjacent mesh cells on either side of the differencing coordinate line with the eigen state determined by adjacent node averages on the difference interval. This scheme has laterally wide support in the difference stencil and thus is not very accurate in high gradient regions and will smear solutions. The other approach splits the side averaged flux difference according to the eigen state at the mesh cell centers. This procedure implies compact differencing schemes and is restrictive. The method also requires a lot of averaging which can be mitigated by placing data nodes at the cell centers. The latter idea is not bad as we shall consider next.

#### Symmetric Methods on Biased Upwind Cells

Additional data nodes at the (body) centers of the natural mesh cells create a symmetric geometric pattern in which the biased upwind cells (Figure 2) of the base level mesh for one coordinate direction are the similarly biased upwind cells in the other coordinate direction of the body centered mesh. Since the nodes of the body centered mesh are centered on the lateral faces of the base mesh upwind cells and visa versa, there is a unique definition of the total flux at the node on every cell face.

For each face of every cell the flux tensor can be decomposed in orthogonal components according to reference directions that may be determined independently from cell to cell. The orthogonal decomposition can be expressed in the unit base vectors  $\hat{\alpha}$  and  $\hat{\beta}$  as

$$F = \hat{\alpha} \hat{\alpha} \bullet F + \hat{\beta} \hat{\beta} \bullet F \equiv F^\alpha + F^\beta \quad (9)$$

We assume the base vectors are related to and generally align with the coordinate lines. Then for either component we can construct the locally one dimensional flux divergence  $\Delta_\alpha \bullet F^\alpha$  according to equation (7) with  $F^\alpha$  replacing  $F_\xi$ . Of course a similar relation is developed for  $\Delta_\beta \bullet F^\beta$  appropriately interchanging the upwind one sided and lateral central difference symbols among  $\xi$  and  $\eta$ .

For either flux divergence component and by analogy with the chain rule CSCM method, generalized flux difference eigenvector splitting may be carried out based on the associated upwind difference interval averaged eigenstate to give

$$\Delta \bullet F^\pm = \hat{A}(I^\pm) \Delta \bullet F \quad (10)$$

Finally associating coordinate  $\xi$  ( $j$ ) with the  $\alpha$  flux tensor component and  $\eta$  ( $k$ ) with  $\beta$ , we can write the flux divergence split implicit method as

$$\begin{aligned} & [\hat{A}(I_\alpha^+ + \Lambda_\alpha^+) \nabla_\xi + \hat{A}(I_\alpha^- + \Lambda_\alpha^-) \Delta_\xi + \hat{B}(I_\beta^+ + \Lambda_\beta^+) \nabla_\eta + \hat{B}(I_\beta^- + \Lambda_\beta^-) \Delta_\eta] \delta q_{j,k} \\ & = -(\hat{A}(I_\alpha^+) \Delta_{j-1} \bullet F^\alpha + \hat{A}(I_\alpha^-) \Delta_j \bullet F^\alpha + \hat{B}(I_\beta^+) \Delta_{k-1} \bullet F^\beta + \hat{B}(I_\beta^-) \Delta_k \bullet F^\beta) \end{aligned} \quad (11)$$

Here, for a two level linearized method, we have via Eq. (5) approximated the split Jacobian matrix  $\tilde{A}^\pm$  by the similarity transform based on the  $\hat{A}$  operator and the associated difference interval estimated eigenvalues

$$\Lambda_\alpha^\pm \simeq [W^\xi, W^\xi, W^\xi + \hat{\xi}C, W^\xi - \hat{\xi}C]^\pm \quad (12)$$

For very skewed meshes, a better estimate of the eigenvalues would be required.

While inherently more accurate, the symmetric staggard grid method described above is seen to closely approximate the chain rule CSCM algorithm. We have given the new derived method the name S-CSCM.

#### Local Total Flux Strong Conservation

Finally we give a simple approach which provides total flux conservation in each computational cell. In the approach we replace in Eq. (5) the partial fluxes by the total flux to give

$$D\delta q = -\hat{A}_\xi^+ \nabla_\xi \bullet \tilde{F} - \hat{A}_\xi^- \Delta_\xi \bullet \tilde{F} - \hat{A}_\eta^+ \nabla_\eta \bullet \tilde{F} - \hat{A}_\eta^- \Delta_\eta \bullet \tilde{F} \quad (13)$$

With Eq. (13) a sufficient (and we would guess necessary) condition for convergence to steady state is that the flux divergence vanish for every computational cell. Within

the total flux divergence framework the subscripts on the symbolic divergence operators  $\nabla_\xi \bullet \tilde{F}$  only serve to identify a kind of cell in the grid. Further, the subscripts  $\xi$  and  $\eta$  on the projection operators serve to identify characteristic directions in which the velocity vectors will be composed in normal and tangential components for advection. When these directions, which we can free from constraint to either or both the curvilinear coordinate directions, are taken to be orthogonal, it can be shown that within truncation errors similar to those for locally one dimensional conservative eigenvector split upwind differencing the method is consistent with the PDE.

Based in an older and independently conceived notion by Roe and Lombard the local cell total flux divergence  $\Delta \bullet \tilde{F}$  can be identified with a residual ("fluctuation", Roe) that is "sent" along grid lines by the method through the projection operators  $\hat{A}_{\xi,\eta}^\pm$  to relax the state at appropriate upwind mesh points. With freedom of the characteristic directions from the grid, we achieve greater freedom in how and where to send residual information.

### Second Order TVD Schemes

For the new locally one dimensional procedure, higher order spatial difference methods for the right hand side of equation (13) can be constructed of the split partial flux divergence by pieced linear combinations of the standard upwind and central difference correction operators. In reference 10, Lombard proposed a simple limiter (Scheme IIIb) for the conservative flux difference split pieces of such a second order method. That limiter by direct analogy can be used here to enhance nonlinear stability. We note that the natural second order method for a scheme constructed of the total flux divergence involves the "Fromm" weights of half central and half upwind.

### Viscous Terms

For both the locally one dimensional and total flux formulations it is feasible following the work of reference 2 to simply add viscous terms in a conventional thin layer central difference formulation. For the locally one dimensional approach this may be appropriate. But from the strong conservation point of view such a practice will interfere with the desirable feature of zeroing the total flux divergence in each computational cell. To preserve that property of the inviscid method, we have only to add the viscous stress terms at the boundaries of the cells such that the terms contribute consistently to the total flux whether or not it is subsequently decomposed into locally one dimensional components.

### Numerical Results

We show here results of computations for a topical difficult propulsion base flow problem of a wind tunnel model tactical missile flow involving realistically complex geometry and flow structure including a centered propulsive jet. The freestream Mach number is 1.4, base diameter  $Re = 0.92 \times 10^6$  and nozzle exit Mach number 2.7 and static pressure ratio of 2.5. The problem has recently been solved with a geometry flexible multiple patched mesh CSCM code – based on the chain rule conservation formulation.

The problem was solved previously by us with an adapted single block mesh code on a double wraparound grid of Figure 3. The grid generated in patches with a simplified algebraic procedure has nice quality over the external and internal corners. But the constrained topology is seen to waste mesh points through excessive clustering in the wake.

The new, better balanced mesh for the present solutions is shown in Figure 4. A plot of the outline of the multiple patch structure of the mesh in the vicinity of the nozzle exit is shown in Figure 5. In the boundary layer region the mesh has an effective wraparound character on an overset patch local to the corner.

We show in Figure 6 a Mach contour plot for the solution on the new mesh. On the whole the better balanced mesh employing about the same number of points produces a result of crisper flow structural detail than the less flexible topology whose solution is shown in Figure 7. Nicely evident in Figure 6 is a weak lip shock, shear layer, barrel shock, (near) contact discontinuity and, above them all, a recompression shock in the external flow.

Lastly in Figure 8, we show a comparison of computational results and experiment. The wave in the base region is due to two counterrotating persistent vortices in the base bubble. We note at the corners a strong qualitative disagreement between solutions on the wraparound grids and a third nonwraparound step mesh<sup>13</sup>. Evidently there the mesh topology strongly influences the mechanism of separation. This point requires further study into topology and mesh refinement.

#### References

1. Lombard, C.K., Oliger, J. and Yang, J.Y., *Lecture Notes in Physics*, 170, pp. 364-370, 1982.
2. Lombard, C.K., Bardina, J., Venkatapathy, E. and Oliger, J., AIAA Paper 83-1895, 1983.
3. Lombard, C.K., Venkatapathy, E. and Bardina, J., AIAA Paper 84-1533, 1984.
4. Bardina, Jorge and Lombard, C.K., AIAA Paper 85-1193, 1985.
5. Roe, P.L., *Lecture Notes in Physics*, 141, pp. 354-359, 1981.
6. Hindman, Richard D., *AIAA J.*, Vol. 20, No. 10, pp. 1359-1367, Oct. 1982.
7. Viviand, H. and Ghazzi, W., *Lecture Notes in Physics*, No. 59, Springer-Verlag, 1976.
8. Lombard, C.K., Davy, W.C. and Green, M.J., AIAA Paper 80-0065, 1980.
9. Vinokur, M., *J. of Computational Physics*, Vol. 14, pp. 105-125, 1974.
10. Yang, J.Y., Lombard, C.K. and Bardina, Jorge, Paper presented at the *International Symposium on Computational Fluid Dynamics-Tokyo*, Sept. 1985.
11. Sahu, J. and Nietubicz, C.J., AIAA Paper 84-0527, 1984.
12. Petrie, H.J. and Walker, B.J., AIAA Paper 85-1618, 1985.
13. Lombard, C.K., Luh, R. C.-C., Nagaraj, N., Bardina, J. and Venkatapathy, E., AIAA Paper 86-0432, 1986.

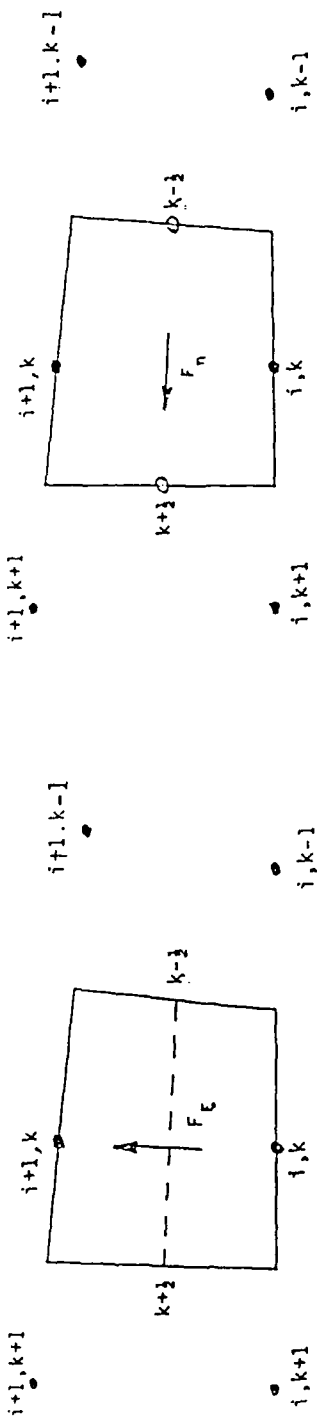


Fig. 1. Computational cell for locally one dimensional coordinate-biased one sided difference method.

Fig. 2. Coordinate biased cells of base grid are also biased n cells of body centered grid.

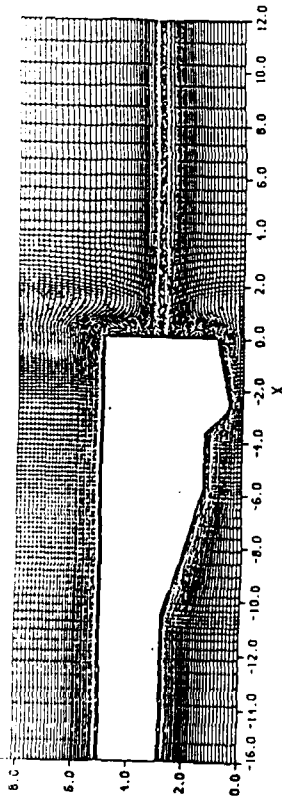


Fig. 3. Double wraparound grid.

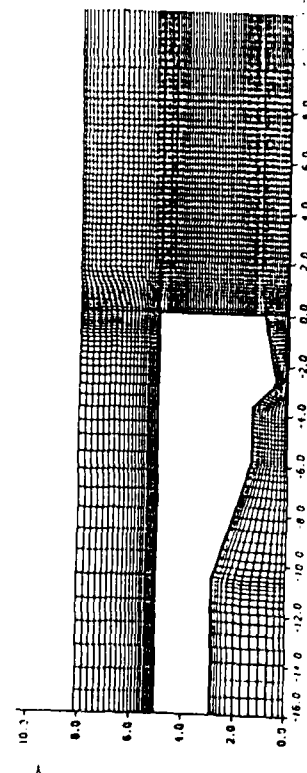


Fig. 4. Multiple patch grid.

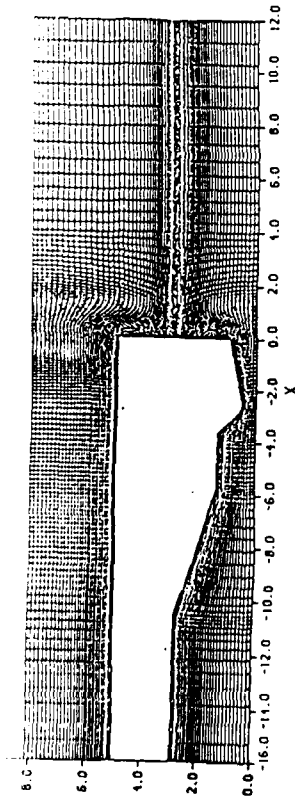


Fig. 5. Overlapping of multiple mesh patches in vicinity of nozzle-base corner.

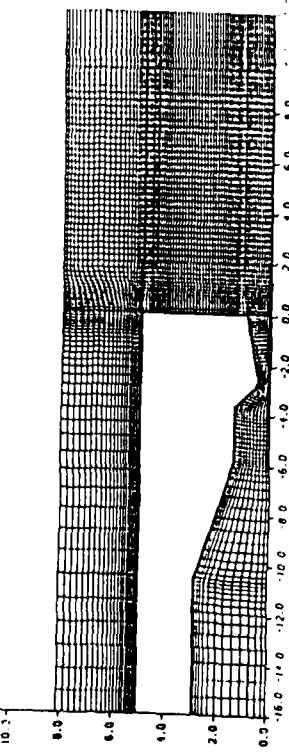


Fig. 6. Mach contour lines for multiple mesh.

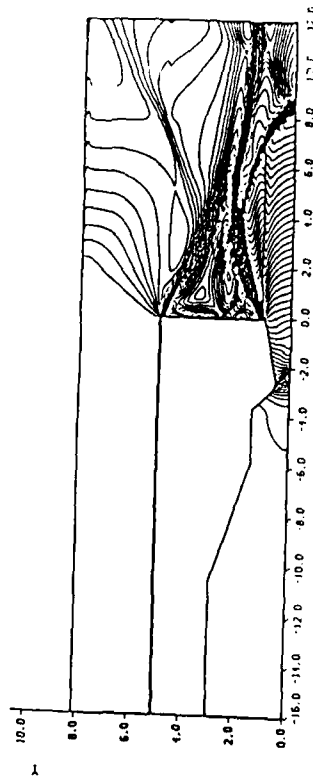


Fig. 7. Mach contour lines for wraparound grid.

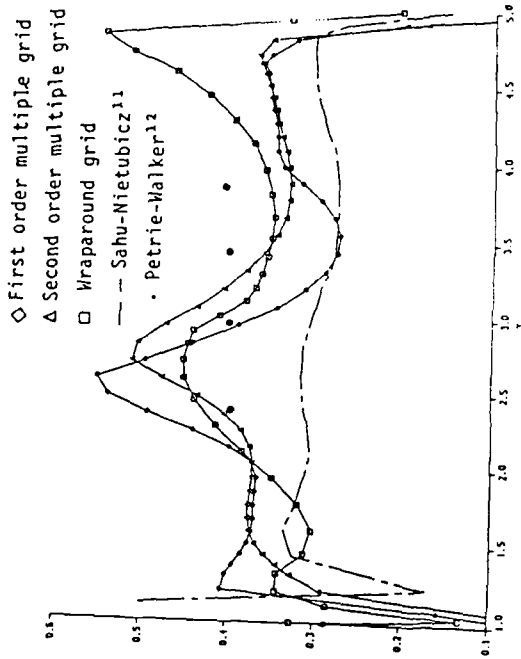


Fig. 8. Base pressure comparison between experiment and numerical solutions.

## 5. Uniformly Second Order Accurate ENO Schemes for the Euler Equations of Gas Dynamics

Very recently, a new class of uniformly high order accurate essentially non-oscillatory (ENO) schemes have been developed by Harten and Osher<sup>1</sup> and Harten et. al.<sup>2-4</sup>. They presented an hierarchy of uniformly high order accurate schemes which generalize Godunov's scheme<sup>5</sup>, and its second order accurate MUSCL extension<sup>6,7</sup> and TVD scheme<sup>8</sup> to arbitrary order of accuracy.

In contrast to the earlier second-order TVD schemes which drop to first-order accuracy at local extrema and maintain second-order accuracy at smooth regions, the new ENO schemes are uniformly high order accurate throughout even at critical points. The ENO schemes use a reconstruction algorithm which is derived from a new interpolation technique that when applied to piecewise smooth data gives high order accuracy whenever the function is smooth but avoids a Gibbs phenomenon at discontinuities. An adaptive stencil of grid points is used; therefore, the resulting schemes are highly nonlinear even in the scalar case.

Theoretical results for the scalar constant coefficient case and numerical results for the scalar conservation law and for the one-dimensional Euler equations of gas dynamics have been reported with highly accurate results. Such high order ENO schemes have the potential to be adapted to the current Euler/Navier-Stokes flow solvers as one does for the TVD schemes to further enhance the accuracy of flowfield simulation. Implementation can be either as a genuine higher-order flow solver as in the present work or as a post-processor to enhance the resolution.

In this paper we first formally extend our second-order TVD schemes described in<sup>9-13</sup> to uniformly second-order ENO schemes for the two-dimensional Euler equations in the general coordinate systems. Both explicit and implicit schemes are described. It is shown that our previous TVD schemes are a special case of the present ENO scheme. Here, the TVD requirement is replaced by a less restricted essentially non-oscillatory condition, a concept advanced by Harten et al<sup>1-4</sup>.

We apply the resulting schemes to simulate complex 2-D gas flows involving multiple discontinuities to test the global accuracy of ENO schemes. In particular, we compare the ENO results directly with the TVD results for the same simulation; thus merits of each method can be assessed.

In Section 2, the two-dimensional Euler equations in the general coordinate system are formulated in the framework<sup>13</sup> of a characteristic flux difference split method. Such methods that we employ are CFDS<sup>14</sup> and CSCM<sup>15</sup>. Properties of the Euler equation which are relevant to the present development are briefly reviewed. To achieve higher order accuracy, a modified flux similar to Harten's is introduced.

In Section 3, we describe a modified flux which can have either an ENO or a TVD property. The relationship between the present approach and Harten-Osher's UNO scheme is illustrated. Both explicit and implicit schemes are described for the 2-D Euler equations in general coordinate systems. Strang-type dimensional splitting<sup>16</sup> is used for explicit methods to simulate time-dependent problems. Standard ADI<sup>17,18</sup> and diagonally dominant ADI<sup>13,15</sup> solution procedures for steady-state calculations are discussed.

Numerical experiments with present ENO schemes for a 1-D shock tube problem, truly nonstationary shock wave diffraction around a cylinder, shock wave collision over a circular arc, and a steady transonic flow over a circular arc in a channel are reported in Section 4. Numerical results are compared with either analytic or experimental results to assess the present work.

Conclusions and suggestions are given in Section 5.

#### Theoretical Considerations

The governing equations of two-dimensional unsteady gas dynamics, neglecting the effects of viscosity and heat transfer, in general curvilinear coordinate systems  $(\xi, \eta)$  are written in conservation form as

$$\partial_t Q + \partial_\xi F + \partial_\eta G = 0 \quad (1)$$

where  $Q = \hat{Q}/J$  and  $F = (\xi_t \hat{Q} + \xi_x \hat{F} + \xi_y \hat{G})/J$ ,  $G = (\eta_t \hat{Q} + \eta_x \hat{F} + \eta_y \hat{G})/J$ , and  $J = \xi_x \eta_y - \xi_y \eta_x$ , the metric Jacobian.  $\hat{Q} = (\rho, \rho u, \rho v, E)^T$  is the conservative variables,  $\hat{F} = (\rho u, \rho u^2 + p, \rho u v, u(E + p))^T$  and  $\hat{G} = (\rho v, \rho v u, \rho v^2 + p, v(E + p))^T$  are the flux vectors in Cartesian coordinates.

Here  $\rho$  is the gas density,  $u, v$  are the gas velocity components,  $E$  the total energy and  $p$  the gas pressure. The pressure is related to other variables by the equation of state, for a perfect gas,  $p = (\gamma - 1)[E - 0.5\rho(u^2 + v^2)]$ , where  $\gamma$  is the specific heats ratio.

Due to the hyperbolicity of system (1), the Jacobian coefficient matrix  $A_\xi = \partial F / \partial Q$  of the transformed equations has real eigenvalues

$$a_1 = U, a_2 = U + c_\xi, a_3 = U, \text{ and } a_4 = U - c_\xi \quad (2)$$

with  $U = \xi_t + \xi_x u + \xi_y v$  and  $c_\xi = c \sqrt{\xi_x^2 + \xi_y^2}$ , where  $c = \sqrt{\gamma p / \rho}$ , is the speed of sound.

One can also find similarity transformation matrices  $T_\xi$  and  $T_\eta$  that diagonalize the system

$$\begin{aligned} T_\xi^{-1} A_\xi T_\xi &= \Lambda_\xi = \text{diag}\{a_i\}, \\ T_\eta^{-1} B_\eta T_\eta &= \Lambda_\eta = \text{diag}\{b_i\} \end{aligned} \quad (3)$$

Since Eq.(1) is a hyperbolic conservation law, both features of hyperbolicity and conservation can be utilized in constructing numerical methods for solving them. A simple and natural way to unify these two aspects is to put Eq.(1) in the following form:

$$\partial_t Q + (\hat{A}_\xi^+ + \hat{A}_\xi^-) \partial_\xi F + (\hat{B}_\eta^+ + \hat{B}_\eta^-) \partial_\eta G = 0 \quad (4)$$

where  $\hat{A}_\xi^\pm$  and  $\hat{B}_\eta^\pm$  are the split normalized Jacobian coefficient matrices that effect the flux difference splitting<sup>13</sup>. Analytic expressions for  $\hat{A}_\xi^\pm$  and  $\hat{B}_\eta^\pm$  are given in Appendix 1.

Several ways of constructing higher-order schemes based on (4) have been investigated<sup>9-11</sup>.

One way to construct a family of second order accurate schemes is to approximate Eq.(4) by

$$\partial_\xi Q + (\hat{A}_\xi^+ + \hat{A}_\xi^-) \partial_\xi F^M + (\hat{B}_\eta^+ + \hat{B}_\eta^-) \partial_\eta G^M = 0 \quad (5)$$

where  $F^M = F + E$  and  $G^M = G + H$  are modified fluxes.

In the following based on Eq.(5), a numerical method of uniformly second order accuracy in time and space which combines both characteristic and conservation features of Eq.(1) is described.

#### Uniformly Second Order Accurate ENO Schemes

Let us define a uniform computational mesh system  $(\xi_j, \eta_k)$  with mesh sizes  $\Delta\xi$ , and  $\Delta\eta$  and let  $Q_{j,k}^n$  denote the value of  $Q$  at time level  $n\Delta\tau$  and at position  $(j\Delta\xi, k\Delta\eta)$ .

A conservative difference scheme for Eq.(5) can be expressed in terms of numerical fluxes  $F^N$  and  $G^N$  as follows:

$$\begin{aligned} \delta Q_{j,k}^n &= Q_{j,k}^{n+1} - Q_{j,k}^n = -\Delta\tau(F_{j+\frac{1}{2},k}^N - F_{j-\frac{1}{2},k}^N) \\ &\quad - \Delta\tau(G_{j,k+\frac{1}{2}}^N - G_{j,k-\frac{1}{2}}^N) \end{aligned} \quad (6)$$

In the following, only the  $L_\xi$  operator is given in detail. Similar expression can be given for the  $L_\eta$  operator. Explicit schemes for Eq.(6) can be constructed by time splitting. For the  $L_\xi$  operator in the  $\xi$ -direction, we have

$$L_\xi Q_{j,k}^n = Q_{j,k}^* = Q_{j,k}^n - \lambda_\xi(F_{j+\frac{1}{2},k}^N - F_{j-\frac{1}{2},k}^N), \quad (7)$$

$$\text{where } \lambda_\xi = \Delta\tau/\Delta\xi$$

In Eq.(7),  $F_{j+\frac{1}{2},k}^N$  is the numerical flux which is given by

$$F_{j+\frac{1}{2},k}^N = F_{j+1,k}^M - \hat{A}_{\xi_{j+\frac{1}{2},k}}^+ \Delta_{j+\frac{1}{2},k} F^M \quad (8a)$$

$$= F_{j,k}^M + \hat{A}_{\xi_{j+\frac{1}{2},k}}^- \Delta_{j+\frac{1}{2},k} F^M \quad (8b)$$

with  $\Delta_{j+\frac{1}{2}}(\cdot) = (\cdot)_{j+1} - (\cdot)_j$ .

In Eq.(8), the split “normalized” Jacobian coefficient matrix  $\hat{A}_\xi^\pm$  satisfies

$$T_\xi^{-1} \hat{A}_\xi^\pm T_\xi = \hat{\Lambda}_\xi^\pm = \text{diag}\{\hat{a}_l^\pm\}, \quad \hat{a}_l^\pm = \frac{1 \pm \text{sgn}(a_l)}{2} \quad (9)$$

The value of  $E$  at nodal point  $j,k$  for the present ENO scheme is  $E_{j,k} = (e_1, e_2, \dots, e_4)_{j,k}^T$  and its  $l$  components

$$\begin{aligned} e_{l,j,k} &= m[\tilde{e}_{l,j+\frac{1}{2},k} - \beta \bar{m}(\Delta_+ \tilde{e}_{l,j+\frac{1}{2},k}, \Delta_- \tilde{e}_{l,j+\frac{1}{2},k}), \tilde{e}_{l,j-\frac{1}{2},k} \\ &\quad + \beta \bar{m}(\Delta_+ \tilde{e}_{l,j-\frac{1}{2},k}, \Delta_- \tilde{e}_{l,j-\frac{1}{2},k})] \end{aligned} \quad (10)$$

where  $\tilde{e}_{l,j+\frac{1}{2},k}$  ( $l = 1, 2, \dots, 4$ ) are components of the column vector

$$\tilde{E}_{j+\frac{1}{2},k} = \operatorname{sgn} A_{\xi,j+\frac{1}{2},k} |(I - \lambda_\xi |A_{\xi,j+\frac{1}{2},k}|) \Delta_{j+\frac{1}{2},k} F|/2 \quad (11)$$

Here  $m$  is the min mod function:

$$\begin{aligned} m(a, b) &= s \min(|a|, |b|) \quad \text{if } \operatorname{sgn} a = \operatorname{sgn} b = s \\ &= 0, \quad \text{otherwise} \end{aligned} \quad (12)$$

The  $\bar{m}$  function is defined as:

$$\begin{aligned} \bar{m}(a, b) &= a \quad \text{if } |a| \leq |b| \\ &= b \quad \text{if } |a| > |b| \end{aligned} \quad (13)$$

For  $\beta = 0.$ , we have a second-order TVD scheme like before. For  $\beta = 0.5$ , we have an uniformly strictly non-oscillatory scheme.

For scalar constant coefficient case, e.g.  $\partial_t u + a \partial_x u = 0$ , Eq.(10) can be proven to be identical to Harten-Osher's non-oscillatory MUSCL-type scheme<sup>1</sup> which uses reconstruction via deconvolution (RD) approach, here of degree 2.

That is

$$\begin{aligned} \bar{R}(x; v^n) &= v_j^n + (x - x_j) \Delta_{j+\frac{1}{2}} v / h \\ &\quad + \frac{1}{2} (x - x_j)(x - x_{j+1}) (s_{j+1} - s_j) / h \\ \text{for } x_j < x < x_{j+1} \end{aligned} \quad (14)$$

with

$$s_j = m\left[\frac{d}{dx} H_2(x_j - 0; v^n), \frac{d}{dx} H_2(x_j + 0; v^n)\right] \quad (15)$$

where  $H_2(x; v)$  is a non-oscillatory piecewise parabolic interpolation.

To further illustrate the present approach and its relationship to Harten-Osher's UNO scheme<sup>1</sup>, let us consider

$$\partial_t u + a \partial_x u = 0, \quad a > 0$$

Then from Eqs.(7), (8) and (10) we have

$$\begin{aligned} v_j^{n+1} &= v_j^n - \sigma \Delta_- v_j^n - \sigma \Delta_- \left( m\left\{\left(\frac{1-\sigma}{2}\right) \Delta_- v_j^n \right. \right. \\ &\quad \left. \left. + \frac{1}{2} \bar{m}\left[\Delta_- \left(\frac{1-\sigma}{2}\right) \Delta_- v_j^n, \Delta_- \left(\frac{1-\sigma}{2}\right) \Delta_+ v_j^n\right], \left(\frac{1-\sigma}{2}\right) \Delta_+ v_j^n \right. \right. \\ &\quad \left. \left. - \frac{1}{2} \bar{m}\left[\Delta_- \left(\frac{1-\sigma}{2}\right) \Delta_+ v_j^n, \Delta_+ \left(\frac{1-\sigma}{2}\right) \Delta_+ v_j^n\right]\right\} \right) \end{aligned} \quad (16)$$

Here  $\sigma = \lambda a$  and it can be a variable. For  $a = 1$ ,  $\sigma = \lambda$ , this reduces to Eq.(4.16) of reference 3.

It is rather constructive to have the scheme written in this form, since one can easily extend that for a single wave equation to a scalar conservation law and to hyperbolic systems of conservation laws in a straightforward manner.

One can similarly construct schemes of higher than second order accuracy for the hyperbolic system of conservation laws. For example, in reference 3, the scheme defined by Eq.(4.19) was obtained using  $N = 3$  in the RP approach.

In Eq.(10), one can replace both of the  $\bar{m}$  by  $m$  to obtain another truly non-oscillatory scheme<sup>1</sup>. For further details of the method, the reader is encouraged to read the original papers<sup>1-4</sup>.

It is noted that the present approach uses a high order representation of the flux vector,  $F_j^M$ , in contrast to the approach defined by Eq.(14) which uses a high order interpolation for the conservative variable  $v_j$ . As a result, the present approach is quite different from that of Harten et al<sup>1-4</sup> for nonlinear cases.

### Implicit Schemes

Implicit schemes can be consistently constructed based on the explicit schemes. An implicit scheme using back Euler in time can be given as

$$[I + \hat{A}^+ \Delta_- A^M + \hat{A}^- \Delta_+ A^M + \hat{B}^+ \Delta_- B^M + \hat{B}^- \Delta_+ B^M] \delta Q^n = RHS \text{ of Eq. (6)} \quad (17)$$

where  $A^M = \partial F^M / \partial Q$  and  $B^M = \partial G^M / \partial Q$ .

In practice we adopt the following approximation

$$\begin{aligned} A^M &= A + \partial E / \partial Q \approx A \\ \text{and } B^M &= B + \partial H / \partial Q \approx B \end{aligned} \quad (18)$$

This corresponds to a linearization procedure and reduces the computational efforts considerably.

### Block Tridiagonal Approximate Factorization

The LHS of equation (17) may be approximately factored in two forms

Standard ADI (Beam and Warming<sup>17,18</sup>)

$$[-A^+, D_\xi, A^-] [-B^+, D_\eta, B^-] \delta Q = RHS \quad (19a)$$

where  $D_\xi = I + |A|$ ,  $D_\eta = I + |B|$  or with reduced errors by

DDADI (Lombard et al<sup>15</sup>)

$$[-A^+, D, A^-] D^{-1} [-B^+, D, B^-] \delta Q \quad (19b)$$

with  $D = I + |A| + |B|$ .

Equations (19) gives the block tridiagonal solution sequences

$$\begin{aligned} [-A^+, D_\xi, A^-]\delta Q^* &= RHS \\ [-B^+, D_\eta, B^-]\delta Q^n &= \delta Q^* \\ Q^{n+1} &= Q^n + \delta Q^n \end{aligned} \quad (20a)$$

and

$$\begin{aligned} [-A^+, D, A^-]\delta Q^* &= RHS \\ [-B^+, D, B^-]\delta Q^n &= D\delta Q^* \\ Q^{n+1} &= Q^n + \delta Q^n \end{aligned} \quad (20b)$$

Implicit TVD schemes with DDADI and bidiagonal approximate factorization have been reported by Yang et al.<sup>13</sup>.

#### Numerical Results and Discussion

Results of several numerical experiments are given in the following. Both unsteady flow using the explicit method and a steady-state solution using the implicit method are included.

##### (1) 1-D shock tube solution

Fig. 1 shows the solution of the 1-D shock tube problem of Sod<sup>19</sup>. Here we have used Eq.(10) with both  $\bar{m}$  replaced by minmod function  $m$ . The same results using a TVD scheme are shown in Fig. 2 for comparison. Moderate improvement at the expansion fan and the contact surface is observed. Slight attenuation is observed for the ENO result which is allowed by the oscillation diminishing property.

##### (2) Shock wave reflection by a circular cylinder

Fig. 3 displays the density contours and Mach number contours for a Mach shock number  $M_s = 2.81$  using the ENO scheme. A comparison with an experimental Schlieren picture is shown in Fig. 4. Excellent agreement is found in nearly every aspect, except for some viscous effects not accounted for by the Euler equations.

##### (3) Shock wave collision over a 15% circular arc

Fig. 5 shows the density, pressure and Mach number contours for two shock waves (with  $M_s = 10$ ,  $\gamma = 1.1$ ) in a head on collision over a circular arc bump using the ENO scheme. The flowfield is very symmetric. The sudden jump in the pressure after the collision can be clearly seen. Multiple Mach shocks (triple shock) and sliplines and their interaction such (vortices) are accurately resolved. Attached leading edge bow shock is observed in contrast to a detached bow shock for  $\gamma = 1.4$ .

##### (4) Asymmetric Shock Wave Collision ( $\gamma = 1.4$ )

Figure 6 displays the post collision flow of a shock wave moving from the right to the left with a delayed shock moving from the left to the right. A vertical contact surface behind the left moving shock (about to exit the frame) and curved bow shocks reflected

from either side are prominent features of the solution. Complicated flow structures such as vortices, multiple Mach shocks and splines can be identified.

The above numerical experiments demonstrate the capability of the present ENO scheme for time-dependent problems; the quality of results is quite good.

Next we consider a steady-state aerodynamic problem using an implicit ENO scheme.

#### (5) GAMM transonic channel flow

We considered one of the standard test cases given at the GAMM Workshop, namely, an internal two-dimensional transonic flow through a parallel channel having a 4.2% thick circular arc at the lower wall. The ratio of static downstream pressure to total pressure is 0.623512, corresponding to  $M_\infty = 0.85$  in the isentropic flow. The  $C_p$  distribution at the lower surface and the Mach number contour plot for the DDADI solution with ENO and TVD schemes are shown in Fig. 7 and Fig. 8, respectively. Both are calculated with  $CFL=10$ . The ENO scheme exhibits superior results to those of the TVD scheme.

#### Concluding Remarks

Uniformly second-order accurate explicit and implicit schemes with the essentially non-oscillatory property have been described for the two-dimensional Euler equations in general curvilinear coordinates. Applications to time-dependent and asymptotic steady-state aerodynamic problems have been carried out. The results exhibit robust stability and high resolution of flowfields involving multiple discontinuities. In comparison with second-order TVD schemes, slight to considerable gain in performance can be achieved for a rather small increase in computational effort depending upon the complexity of the flowfields involved. One of the main objectives is to test the new ENO scheme, which has a completely different underlying design principle in practical aerodynamic applications. Numerical experiments suggest that potential benefit can be gained with this new class of high order essentially non-oscillatory schemes. Extension to include the viscous terms for the Navier-Stokes equations can be accomplished in a standard manner using central differencing. Such implementation is currently underway.

#### References

1. Harten, A., Osher, S., "Uniformly High-Order Accurate Non-Oscillatory Schemes, I." MRC Technical Summary Report No. 2823, May 1985. to appear in SINUM.
2. Harten, A., Engquist, B., Osher, S., Chakravathy, S.R., "Uniformly High Order Accurate Essentially Non-Oscillatory Schemes II" (in preparation).
3. Harten, A., Engquist, B., Osher, S., and Chakravathy, S.R., "Some Results on Uniformly High-Order Accurate Essentially Non-Oscillatory Schemes", in *Advances in Numerical Analysis and Applied Mathematics*, Eds. J. C. South, JR. and M.Y. Hussaini, ICASE Report 86-18, also to appear in *J. App. Num. Math.*
4. Harten, A., Engquist, B., Osher, S., and Chakravathy, S.R., "Uniformly High Order Accurate Essentially Non-Oscillatory Schemes III.", ICASE Report 86-22 April 1986.
5. Godunov, S.K., "A Finite Difference Method for the Numerical Computation of Discontinuous Solutions of the Equations to Fluid Dynamics," *Mat. Sb.*, 47 (1959) pp. 271-290.

6. B. van Leer, "Towards the Ultimate Conservative Difference Schemes V. A Second Order Sequel to Godunov's Method," *J. Comp. Phys.*, vol. 32, (1979) pp. 101-136
7. Colella, P., and Woodward, P.R., "The Piecewise-Parabolic Method (PPM) for Gas-Dynamical Simulations," *J. Comp. Phys.*, vol. 54 (1984), pp. 174-201
8. Harten, A., "High resolution Schemes for Hyperbolic Conservation Laws," *J. Comp. Phys.*, vol. 49 (1983), pp. 357-393.
9. Yang, J. Y., "Second- and Third-Order Upwind Flux Difference Splitting Schemes for the Euler Equations," NASA TM-85959, July, 1984.
10. Yang, J. Y., "Numerical Solution of the Two-Dimensional Euler Equations by Second-Order Upwind Difference Schemes," AIAA Paper 85-0292, AIAA 23rd Aerospace Sciences Meeting, Reno, 1985.
11. Yang, J. Y., "Higher-Order Flux Difference Splitting Schemes for the Euler Equations Using Upstream Interpolations," Proc 6th GAMM Conf. on Numerical Methods in Fluid Mechanics, Göttingen, September 1985.
12. Yang, J.Y., Y. Liu, and H. Lomax, "Computation of Shock Wave Reflection by Circular Cylinders," AIAA Paper 86-0272, 1986. To appear in *AIAA J.*.
13. Yang, J.Y. Lombard, C.K., and Bardina, J., "Implicit TVD Schemes for the Euler Equations with Bidiagonal Approximate Factorization," *International Symposium on Computational Fluid Dynamics, Tokyo, Japan*, vol. 1 (1985) pp. 239-250.
14. Yang, J.Y., Lombard, C.K. and Bershad, D., "A Characteristic Flux Difference Splitting for the Hyperbolic Conservation Laws of Gas Dynamics," AIAA-83-0040, 1983.
15. Lombard, C.K. Bardina, J. Venkatapathy, E. and Oliger J., "Multi-Dimensional Formulation of CSCM-An Upwind Flux Difference Eigenvector Split Method for the Compressible Navier-Stokes Equations," AIAA 83-1895, 1983.
16. Strang, G., "On the Construction and Comparison of Difference Schemes," SINUM, Vol. 5, (1968) pp. 506-517.
17. Warming R.F. and Beam R.M., "On Construction and Application of Implicit Factored Schemes for Conservation Laws," SIAM-AMS Proceedings, Vol. II, 1977.
18. Beam R.M. and Warming R.F., "An Implicit Factored Scheme for the Compressible Navier-Stokes Equations," *AIAA Journal*, vol. 16, (1978) pp. 393-401.
19. Sod, G. A., "A Survey of Several Finite Difference Methods for Systems of Nonlinear Hyperbolic Conservation Laws," *J. Comp. Phys.*, vol. 27 (1978) pp. 1-31.

#### Appendix

Analytical expressions for  $\hat{A}_\epsilon^\pm$  and  $\hat{B}_\eta^\pm$ .

$$\begin{aligned}\hat{a}_{11}^\pm &= \hat{\lambda}_1^\pm - \left( \frac{\hat{\lambda}_2^\pm - \hat{\lambda}_3^\pm}{2} \right) (\tilde{\xi}_x u + \tilde{\xi}_y v) / c \\ &\quad + \left( \frac{\hat{\lambda}_2^\pm + \hat{\lambda}_3^\pm}{2} - \hat{\lambda}_1^\pm \right) (\gamma - 1) \left( \frac{u^2 + v^2}{2} \right) / c^2\end{aligned}$$

$$\hat{a}_{12}^{\pm} = \left(\frac{\hat{\lambda}_2^{\pm} - \hat{\lambda}_3^{\pm}}{2}\right)\tilde{\xi}_x/c - \left(\frac{\hat{\lambda}_2^{\pm} + \hat{\lambda}_3^{\pm}}{2} - \hat{\lambda}_1^{\pm}\right)(\gamma - 1)u/c^2$$

$$\hat{a}_{13}^{\pm} = \left(\frac{\hat{\lambda}_2^{\pm} - \hat{\lambda}_3^{\pm}}{2}\right)\tilde{\xi}_y/c - \left(\frac{\hat{\lambda}_2^{\pm} + \hat{\lambda}_3^{\pm}}{2} - \hat{\lambda}_1^{\pm}\right)(\gamma - 1)v/c^2$$

$$\hat{a}_{14}^{\pm} = \left(\frac{\hat{\lambda}_2^{\pm} + \hat{\lambda}_3^{\pm}}{2} - \hat{\lambda}_1^{\pm}\right)(\gamma - 1)/c^2$$

$$\begin{aligned}\hat{a}_{21}^{\pm} &= \left(\frac{\hat{\lambda}_2^{\pm} + \hat{\lambda}_3^{\pm}}{2} - \hat{\lambda}_1^{\pm}\right)(\gamma - 1)u\left(\frac{u^2 + v^2}{2}\right)/c^2 \\ &+ \left(\frac{\hat{\lambda}_2^{\pm} - \hat{\lambda}_3^{\pm}}{2}\right)(\gamma - 1)\left(\frac{u^2 + v^2}{2}\right)\tilde{\xi}_x/c - \left(\frac{\hat{\lambda}_2^{\pm} + \hat{\lambda}_3^{\pm}}{2}\right)(\tilde{\xi}_x u + \tilde{\xi}_y v)u/c \\ &- \left(\frac{\hat{\lambda}_2^{\pm} + \hat{\lambda}_3^{\pm}}{2} - \hat{\lambda}_1^{\pm}\right)(\tilde{\xi}_x u + \tilde{\xi}_y v)\tilde{\xi}_x\end{aligned}$$

$$\begin{aligned}\hat{a}_{22}^{\pm} &= \hat{\lambda}_1^{\pm} + \left(\frac{\hat{\lambda}_2^{\pm} + \hat{\lambda}_3^{\pm}}{2} - \hat{\lambda}_1^{\pm}\right)\tilde{\xi}_x^2 \\ &- \left(\frac{\hat{\lambda}_2^{\pm} + \hat{\lambda}_3^{\pm}}{2} - \hat{\lambda}_1^{\pm}\right)(\gamma - 1)u^2/c^2 - \left(\frac{\hat{\lambda}_2^{\pm} - \hat{\lambda}_3^{\pm}}{2}\right)(\gamma - 2)\tilde{\xi}_x u/c\end{aligned}$$

$$\begin{aligned}\hat{a}_{23}^{\pm} &= \left(\frac{\hat{\lambda}_2^{\pm} - \hat{\lambda}_3^{\pm}}{2}\right)\tilde{\xi}_y u/c - \left(\frac{\hat{\lambda}_2^{\pm} + \hat{\lambda}_3^{\pm}}{2} - \hat{\lambda}_1^{\pm}\right)(\gamma - 1)uv/c^2 \\ &+ \left(\frac{\hat{\lambda}_2^{\pm} + \hat{\lambda}_3^{\pm}}{2} - \hat{\lambda}_1^{\pm}\right)\tilde{\xi}_x \tilde{\xi}_y - \left(\frac{\hat{\lambda}_2^{\pm} - \hat{\lambda}_3^{\pm}}{2}\right)(\gamma - 1)\tilde{\xi}_x v/c\end{aligned}$$

$$\hat{a}_{24}^{\pm} = \left(\frac{\hat{\lambda}_2^{\pm} + \hat{\lambda}_3^{\pm}}{2} - \hat{\lambda}_1^{\pm}\right)(\gamma - 1)u/c^2 + \left(\frac{\hat{\lambda}_2^{\pm} - \hat{\lambda}_3^{\pm}}{2}\right)(\gamma - 1)\tilde{\xi}_x/c$$

$$\begin{aligned}\hat{a}_{31}^{\pm} &= \hat{\lambda}_1^{\pm}v - \left(\frac{\hat{\lambda}_2^{\pm} - \hat{\lambda}_3^{\pm}}{2}\right)(\tilde{\xi}_x u + \tilde{\xi}_y v)v/c \\ &+ \left(\frac{\hat{\lambda}_2^{\pm} + \hat{\lambda}_3^{\pm}}{2} - \hat{\lambda}_1^{\pm}\right)(\gamma - 1)\left(\frac{u^2 + v^2}{2}\right)v/c^2 \\ &- \left(\frac{\hat{\lambda}_2^{\pm} + \hat{\lambda}_3^{\pm}}{2} - \hat{\lambda}_1^{\pm}\right)\tilde{\xi}_x \tilde{\xi}_y u - [\hat{\lambda}_1^{\pm}\tilde{\xi}_x^2 + \left(\frac{\hat{\lambda}_2^{\pm} + \hat{\lambda}_3^{\pm}}{2}\right)\tilde{\xi}_y^2]v \\ &+ \left(\frac{\hat{\lambda}_2^{\pm} - \hat{\lambda}_3^{\pm}}{2}\right)(\gamma - 1)\left(\frac{u^2 + v^2}{2}\right)\tilde{\xi}_y/c\end{aligned}$$

$$\begin{aligned}\hat{a}_{32}^{\pm} &= \left(\frac{\hat{\lambda}_2^{\pm} - \hat{\lambda}_3^{\pm}}{2}\right)\tilde{\xi}_x v/c - \left(\frac{\hat{\lambda}_2^{\pm} + \hat{\lambda}_3^{\pm}}{2} - \hat{\lambda}_1^{\pm}\right)(\gamma - 1)uv/c^2 \\ &+ \left(\frac{\hat{\lambda}_2^{\pm} + \hat{\lambda}_3^{\pm}}{2} - \hat{\lambda}_1^{\pm}\right)\tilde{\xi}_x \tilde{\xi}_y - \left(\frac{\hat{\lambda}_2^{\pm} - \hat{\lambda}_3^{\pm}}{2}\right)(\gamma - 1)\tilde{\xi}_y u/c\end{aligned}$$

$$\begin{aligned}
\hat{a}_{33}^{\pm} &= \left(\frac{\hat{\lambda}_2^{\pm} - \hat{\lambda}_3^{\pm}}{2}\right)(2 - \gamma)\tilde{\xi}_y v/c \\
&\quad - \left(\frac{\hat{\lambda}_2^{\pm} + \hat{\lambda}_3^{\pm}}{2} - \hat{\lambda}_1^{\pm}\right)(\gamma - 1)v^2/c^2 + \hat{\lambda}_1^{\pm}\tilde{\xi}_x^2 + \left(\frac{\hat{\lambda}_2^{\pm} + \hat{\lambda}_3^{\pm}}{2}\right)\tilde{\xi}_y^2 \\
\hat{a}_{34}^{\pm} &= \left(\frac{\hat{\lambda}_2^{\pm} + \hat{\lambda}_3^{\pm}}{2} - \hat{\lambda}_1^{\pm}\right)(\gamma - 1)v/c^2 + \left(\frac{\hat{\lambda}_2^{\pm} - \hat{\lambda}_3^{\pm}}{2}\right)(\gamma - 1)\tilde{\xi}_y/c \\
\hat{a}_{41}^{\pm} &= \left(\hat{\lambda}_1^{\pm} + \frac{\hat{\lambda}_2^{\pm} + \hat{\lambda}_3^{\pm}}{2}\right)\left(\frac{u^2 + v^2}{2}\right) \\
&\quad - \left(\frac{\hat{\lambda}_2^{\pm} - \hat{\lambda}_3^{\pm}}{2}\right)(2 - \gamma)(\tilde{\xi}_x u + \tilde{\xi}_y v)\left(\frac{u^2 + v^2}{2}\right)/c \\
&\quad + \left(\frac{\hat{\lambda}_2^{\pm} + \hat{\lambda}_3^{\pm}}{2} - \hat{\lambda}_1^{\pm}\right)(\gamma - 1)\left(\frac{u^2 + v^2}{2}\right)^2/c^2 \\
&\quad - \left(\frac{\hat{\lambda}_2^{\pm} - \hat{\lambda}_3^{\pm}}{2}\right)(\tilde{\xi}_x u + \tilde{\xi}_y v)c/(\gamma - 1) \\
&\quad - \left(\frac{\hat{\lambda}_2^{\pm} + \hat{\lambda}_3^{\pm}}{2}\right)(\tilde{\xi}_x u + \tilde{\xi}_y v)^2 - \hat{\lambda}_1^{\pm}(\tilde{\xi}_y u - \tilde{\xi}_x v)^2 \\
\hat{a}_{42}^{\pm} &= \left(\frac{\hat{\lambda}_2^{\pm} - \hat{\lambda}_3^{\pm}}{2}\right)\tilde{\xi}_x\left(\frac{u^2 + v^2}{2}\right)/c \\
&\quad - \left(\frac{\hat{\lambda}_2^{\pm} + \hat{\lambda}_3^{\pm}}{2} - \hat{\lambda}_1^{\pm}\right)(\gamma - 1)u\left(\frac{u^2 + v^2}{2}\right)/c^2 \\
&\quad - \left(\frac{\hat{\lambda}_2^{\pm} - \hat{\lambda}_3^{\pm}}{2}\right)(\gamma - 1)u(\tilde{\xi}_x u + \tilde{\xi}_y v)/c \\
&\quad + \left(\frac{\hat{\lambda}_2^{\pm} - \hat{\lambda}_3^{\pm}}{2}\right)\tilde{\xi}_x c/(\gamma - 1) - \left(\frac{\hat{\lambda}_2^{\pm} + \hat{\lambda}_3^{\pm}}{2} - \hat{\lambda}_1^{\pm}\right)\tilde{\xi}_y^2 u \\
&\quad + \left(\frac{\hat{\lambda}_2^{\pm} + \hat{\lambda}_3^{\pm}}{2} - \hat{\lambda}_1^{\pm}\right)\tilde{\xi}_x \tilde{\xi}_y v \\
\hat{a}_{43}^{\pm} &= \left(\frac{\hat{\lambda}_2^{\pm} - \hat{\lambda}_3^{\pm}}{2}\right)\tilde{\xi}_x\left(\frac{u^2 + v^2}{2}\right)/c \\
&\quad - \left(\frac{\hat{\lambda}_2^{\pm} + \hat{\lambda}_3^{\pm}}{2} - \hat{\lambda}_1^{\pm}\right)(\gamma - 1)v\left(\frac{u^2 + v^2}{2}\right)/c^2 \\
&\quad + \left(\frac{\hat{\lambda}_2^{\pm} + \hat{\lambda}_3^{\pm}}{2} - \hat{\lambda}_1^{\pm}\right)\tilde{\xi}_x \tilde{\xi}_y u \\
&\quad - \left(\frac{\hat{\lambda}_2^{\pm} + \hat{\lambda}_3^{\pm}}{2} - \hat{\lambda}_1^{\pm}\right)\tilde{\xi}_x^2 v + \left(\frac{\hat{\lambda}_2^{\pm} - \hat{\lambda}_3^{\pm}}{2}\right)\tilde{\xi}_y c/(\gamma - 1) \\
&\quad - \left(\frac{\hat{\lambda}_2^{\pm} - \hat{\lambda}_3^{\pm}}{2}\right)(\gamma - 1)v(\tilde{\xi}_x u + \tilde{\xi}_y v)/c
\end{aligned}$$

$$\hat{a}_{44}^{\pm} = \left( \frac{\hat{\lambda}_2^{\pm} + \hat{\lambda}_3^{\pm}}{2} \right) + \left( \frac{\hat{\lambda}_2^{\pm} + \hat{\lambda}_3^{\pm}}{2} - \hat{\lambda}_1^{\pm} \right) (\gamma - 1) \left( \frac{u^2 + v^2}{2} \right) / c^2$$

$$+ \left( \frac{\hat{\lambda}_2^{\pm} - \hat{\lambda}_3^{\pm}}{2} \right) (\gamma - 1) (\tilde{\xi}_x u + \tilde{\xi}_y v) / c$$

The expressions for  $\hat{B}_{\eta}^{\pm}$  are obtained by replacing  $\tilde{\xi}_x$  and  $\tilde{\xi}_y$  by  $\tilde{\eta}_x$  and  $\tilde{\eta}_y$ , respectively.

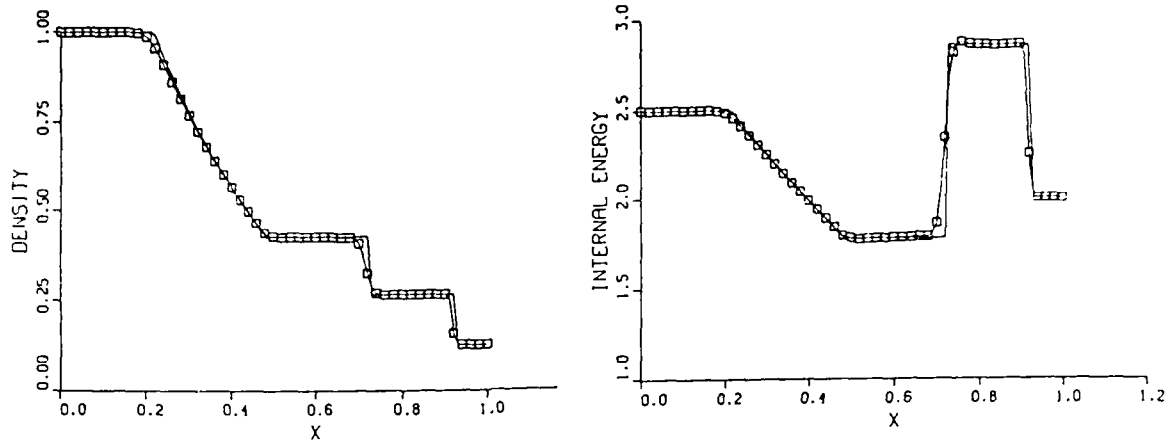


Figure 1. 1-D shock tube solution with ENO scheme.

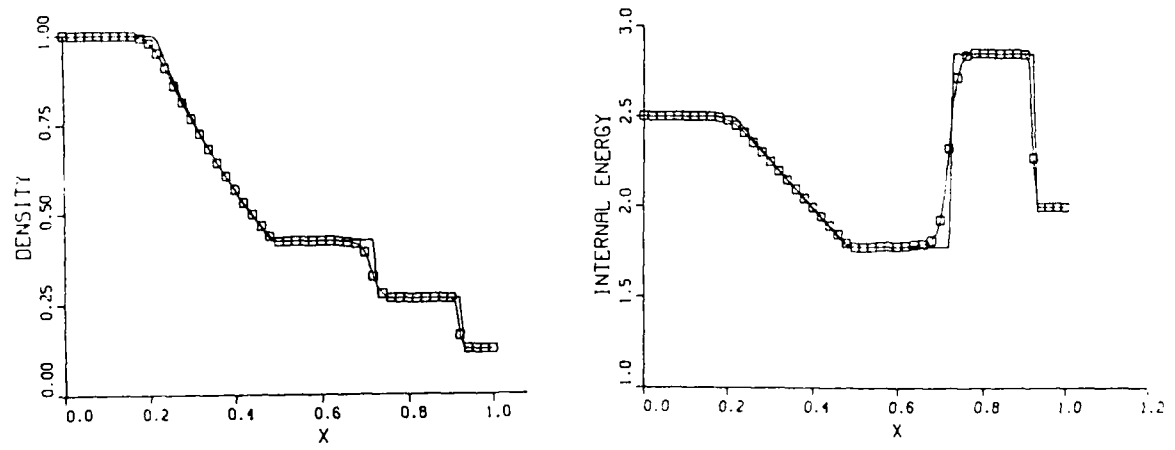


Figure 2. 1-D shock tube solution with TVD scheme.

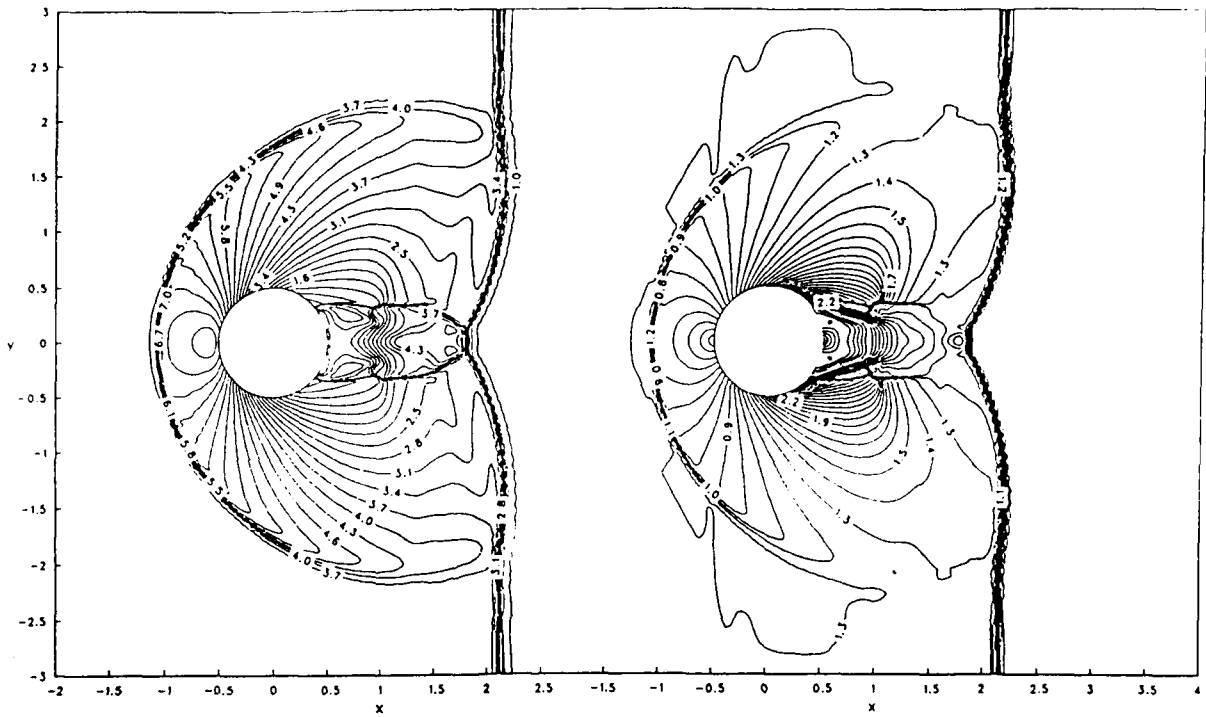


Figure 3. Shock waves reflection around cylinder by explicit ENO scheme ( $M_s = 2.81$ ). (a) Density contours. (b) Mach number contours.

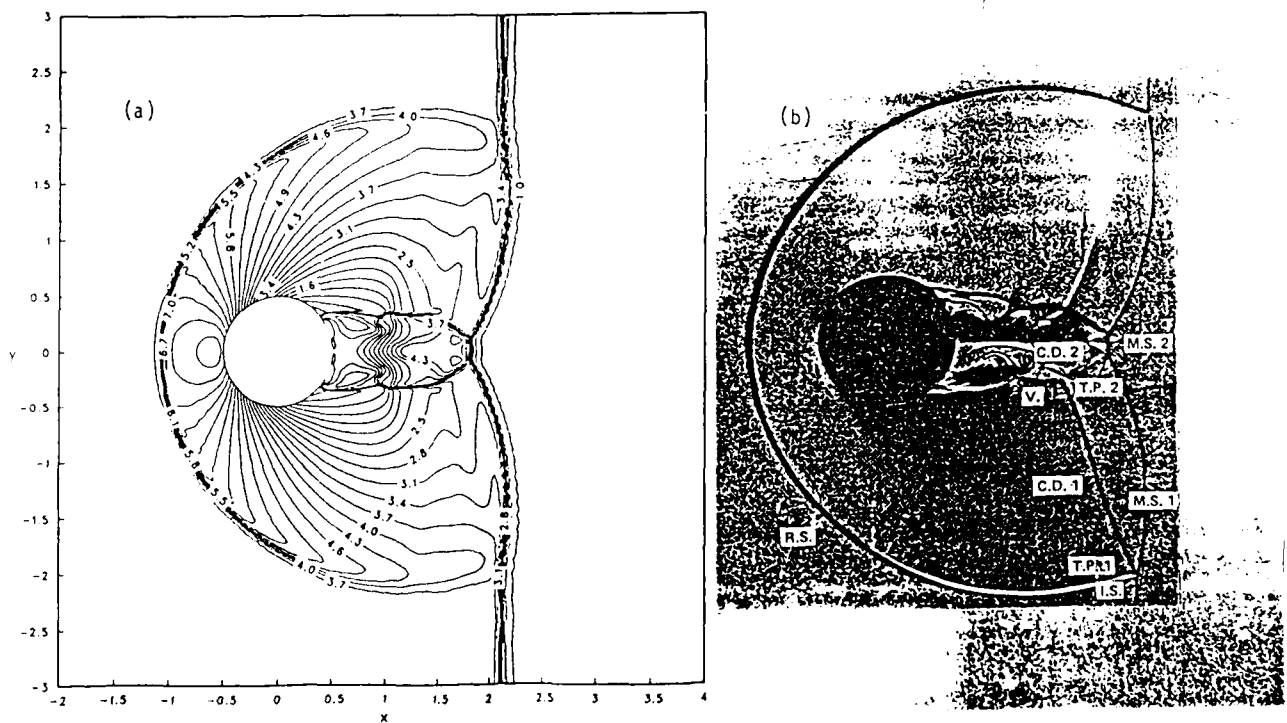


Figure 4. Shock wave reflection around cylinder by the ENO scheme. (a) Computation. (b) Experimental Schlieren picture.

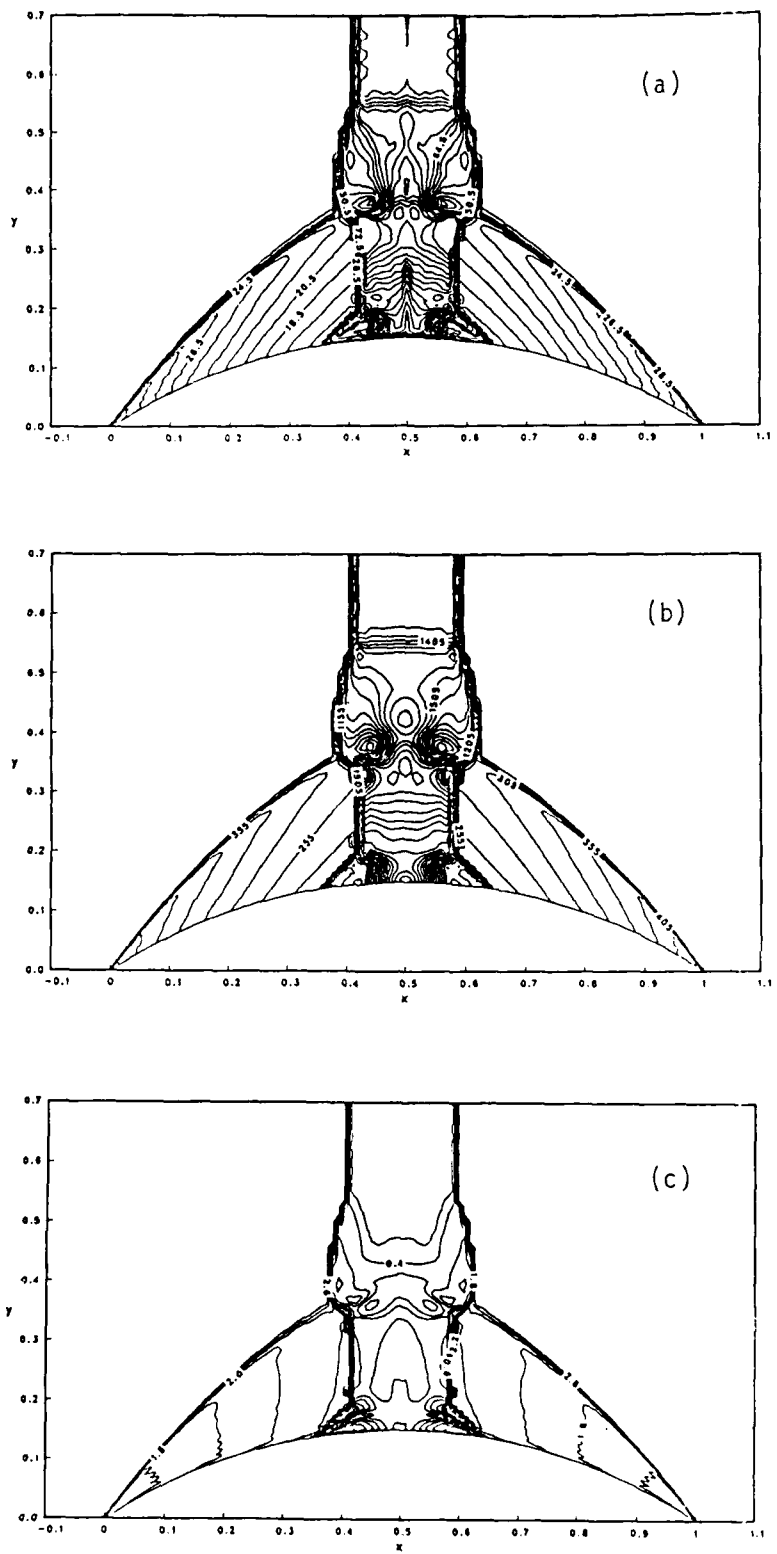


Figure 5. Time dependent symmetric shock diffraction - collision over circular arc airfoil. (a) Density contours. (b) Pressure contours. (c) Mach number contours.

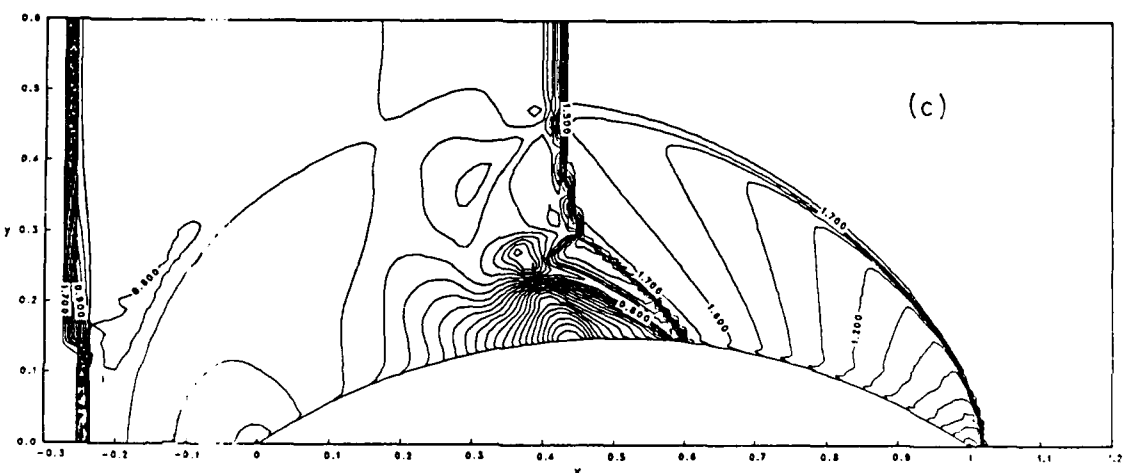
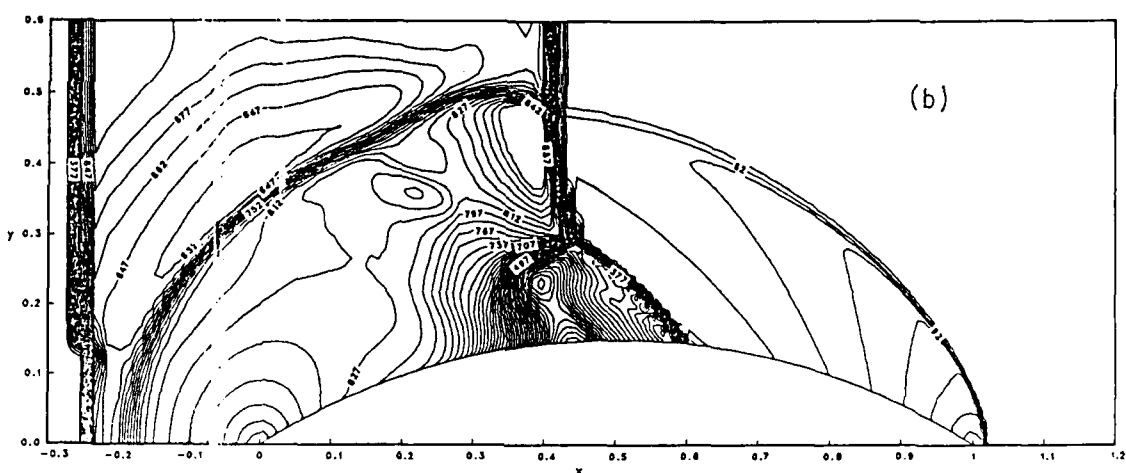
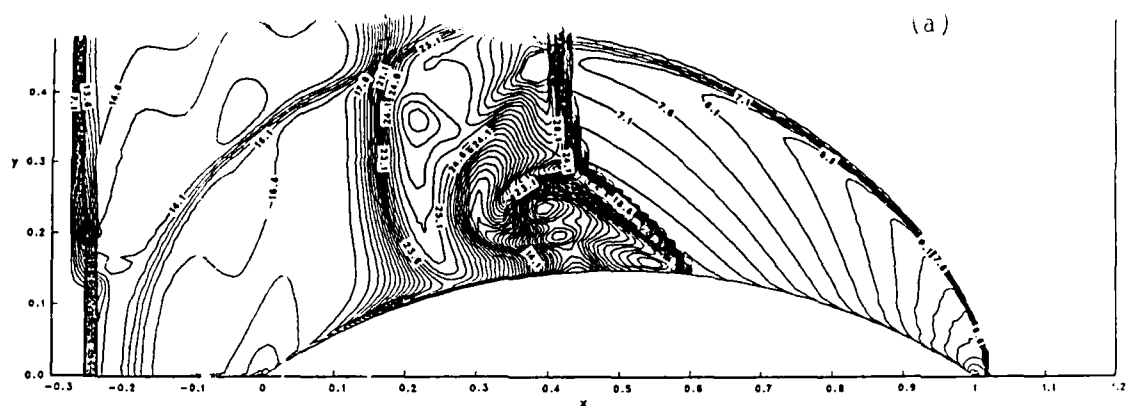


Figure 6. Time dependent asymmetric shock diffraction - collision over circular arc airfoil. (a) Density contours. (b) Pressure contours. (c) Mach number contours.

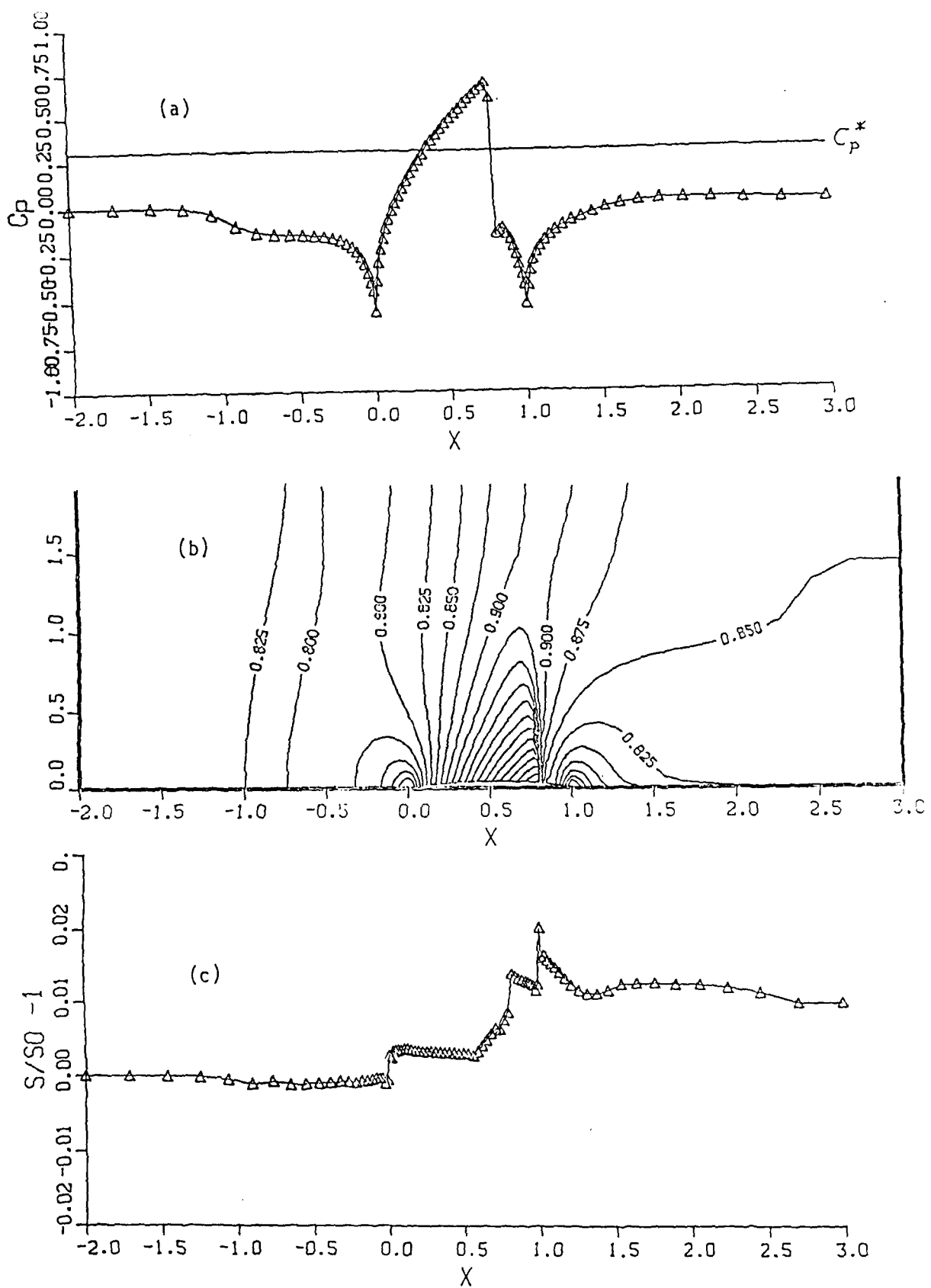


Fig. 7 Solution of GAMM transonic channel flow with DDADI TVD scheme. (a)  $C_p$  distribution at lower surface. (b) Mach number contours (c) Entropy distribution at lower surface.

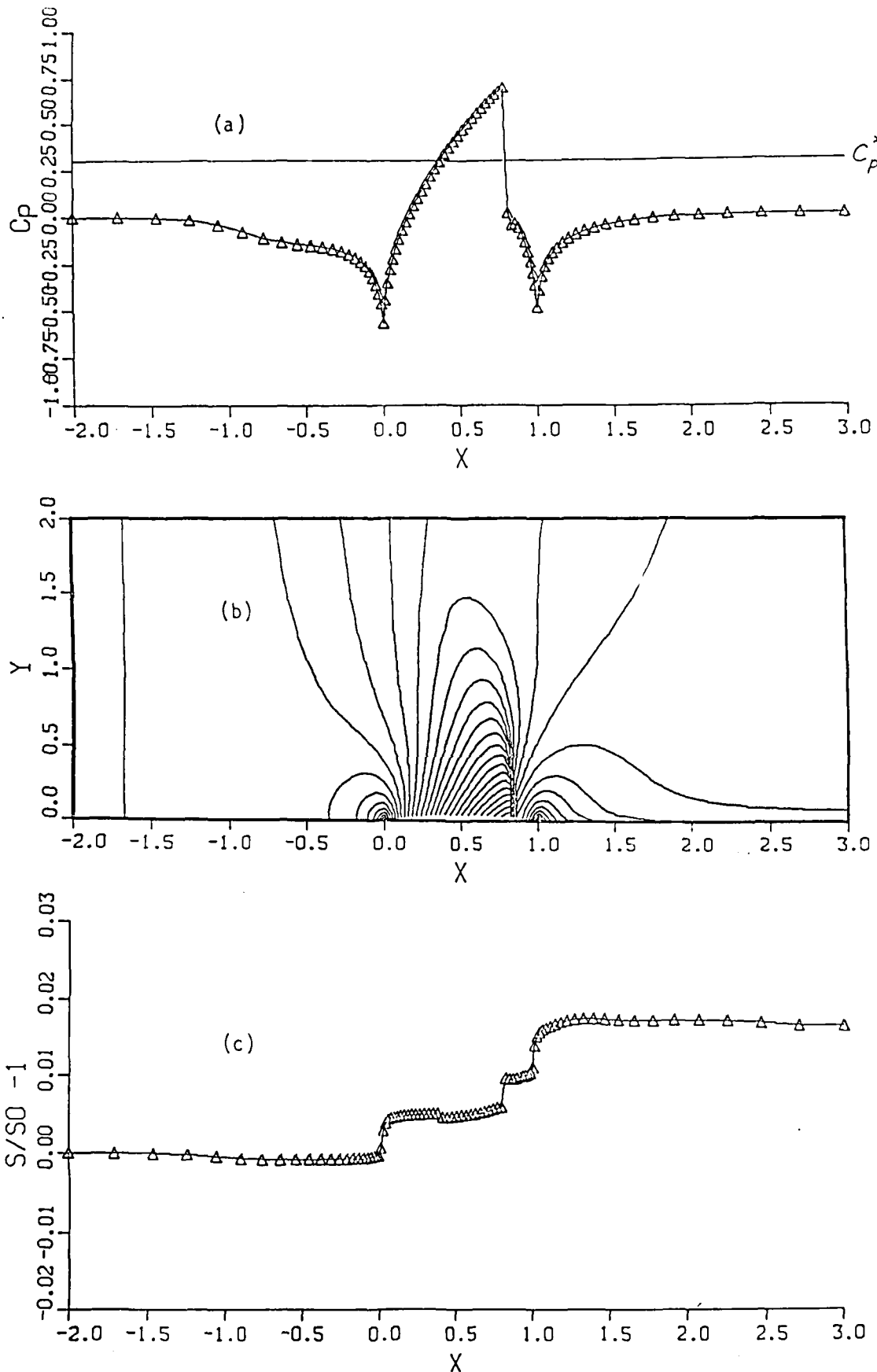


Fig. 8 Solution of the GAMM transonic channel flow with DDADI ENO scheme. (a)  $C_p$  distribution (b) Mach number contour (c) Entropy distribution at lower surface.

## 6. Three Dimensional Hypersonic Shock Capturing CSCM Upwind Implicit Navier-Stokes Method

The effective engineering design of the new transatmospheric space vehicles flying at hypersonic speeds requires computational aerothermodynamics (CAT) technology in the frontier of present scientific research<sup>1</sup>. The aeroassisted orbital transfer vehicle (AOTV) to fly at Mach 30 in the upper atmosphere has the design requirement to predict the large low speed zone of recirculating flow with the turbulent wake behind this vehicle and represents a major research activity. Another major hypersonic vehicle under current investigation is the transatmospheric vehicle (TAV) which will fly into orbit from Earth's surface and land back using its own power. The design of these vehicles will require the integration of different areas of technology. In particular, the combination of an efficient three dimensional shock capturing CFD method such as the 3-D CSCM upwind method<sup>2</sup> with an efficient nonequilibrium chemistry procedure<sup>3</sup> is needed to account for the significant effects of thinner shock layer on drag and wall heat transfer associated with high altitude hypervelocity flight.

The 3-D CSCM algorithm employed here is an implicit method of planes symmetric Gauss-Seidel relaxation scheme<sup>4</sup>. The data is conveniently stored on successive planes along the streamwise coordinate, and the system of equations is iterated, i.e. solved twice, in marching successive planes of the streamwise coordinate; along the forward direction, first, and along the backward direction, afterwards. In each plane the solution is obtained by a two level pseudo time dependent relaxation procedure based on the diagonally dominant approximate factorization DDADI<sup>5</sup>. The space marching alternating directional sweeps in the streamwise coordinate are von Neumann unconditionally stable<sup>6,7,8</sup> for zones of subsonic and streamwise separated and reversed flows as well as supersonic flow. Much as do the more restrictive PNS techniques, the present space marching method results in improved propagation of nonlinear advection to accelerate convergence to steady state.

The relaxation algorithm has half the storage requirements and substantially accelerated convergence over related two level linearized time dependent implicit methods. The method also requires only a few 2-D cross-flow data planes in core at any marching step and thus with fast disc storage, such as is available on the CRAY-XMP machines, can efficiently treat complex problems requiring very large numbers of mesh points in 3-D. Accordingly the method provides a base where chemistry procedures can efficiently be exploited.

The purpose of this present report is to describe important features of the 3-D CSCM shock capturing method for hypersonic flow, and to show the performance of the method in the simulation of the hypersonic equilibrium flowfield around a sphere-cone-cone-flare reentry vehicle (RV) at angle of attack. The present work for perfect gases has recently been extended to flows of general equilibrium chemically reacting gases by Nagaraj, et al<sup>9</sup>. The 3-D code is substantially validated by comparison with results in axisymmetric flow for the generically similar 2-D/axisymmetric CSCM upwind code that has previously been extensively tested against experiment in both external and internal flows as described in

the referenced works. For both classes of flows CSCM has demonstrated convective heat transfer capability<sup>10</sup>.

In the following sections we will first describe the numerical method and then present the numerical results.

### CSCM Gasdynamic Formulation

The conservative finite volume finite difference formulation of the 3-D compressible Navier-Stokes equations in general curvilinear coordinates  $\xi(x, y, z)$ ,  $\eta(x, y, z)$ , and  $\psi(x, y, z)$  is expressed as

$$\begin{aligned} \tilde{J} \partial_t q + \tilde{\xi}_x \partial_\xi F + \tilde{\xi}_y \partial_\xi G + \tilde{\xi}_z \partial_\xi H + \\ \tilde{\eta}_x \partial_\eta F + \tilde{\eta}_y \partial_\eta G + \tilde{\eta}_z \partial_\eta H + \\ \tilde{\psi}_x \partial_\psi F + \tilde{\psi}_y \partial_\psi G + \tilde{\psi}_z \partial_\psi H = 0 \end{aligned} \quad (1)$$

where  $F$ ,  $G$ , and  $H$  are the flux vectors in the Cartesian coordinate directions  $x$ ,  $y$ ,  $z$ , respectively; while  $q$  represents the conservative dependent variables,

$$q = (\rho, \rho u, \rho v, \rho w, e) \quad (2)$$

$$\begin{aligned} F = (\rho u, \rho u^2 + p - \sigma_{xx}, \rho uv - \tau_{xy}, \rho uw - \tau_{xz}, \\ (e + p)u - u\sigma_{xx} - v\tau_{xy} - w\tau_{xz} - \kappa T_x) \end{aligned} \quad (3)$$

$$\begin{aligned} G = (\rho v, \rho uv - \tau_{yx}, \rho v^2 + p - \sigma_{yy}, \rho vw - \tau_{yz}, \\ (e + p)v - u\tau_{yx} - v\sigma_{yy} - w\tau_{yz} - \kappa T_y) \end{aligned} \quad (4)$$

$$\begin{aligned} H = (\rho w, \rho uw - \tau_{zx}, \rho vw - \tau_{zy}, \rho w^2 + p - \sigma_{zz}, \\ (e + p)w - u\tau_{zx} - v\tau_{zy} - w\sigma_{zz} - \kappa T_z) . \end{aligned} \quad (5)$$

### Metric Coefficients

The metric coefficients of the generalized coordinate transformation (1) are computed numerically as the difference interval averages of the mesh point functions.

$$\begin{pmatrix} \tilde{\xi}_x & \tilde{\xi}_y & \tilde{\xi}_z \\ \tilde{\eta}_x & \tilde{\eta}_y & \tilde{\eta}_z \\ \tilde{\psi}_x & \tilde{\psi}_y & \tilde{\psi}_z \end{pmatrix}$$

$$= \begin{pmatrix} y_\eta z_\psi - z_\eta y_\psi & z_\eta x_\psi - x_\eta z_\psi & x_\eta y_\psi - y_\eta x_\psi \\ y_\psi z_\xi - z_\psi y_\xi & z_\psi x_\xi - x_\psi z_\xi & x_\psi y_\xi - y_\psi x_\xi \\ y_\xi z_\eta - z_\xi y_\eta & z_\xi x_\eta - x_\xi z_\eta & x_\xi y_\eta - y_\xi x_\eta \end{pmatrix} \quad (6)$$

In the numerical method the expressions on the right hand side of equations (6) are evaluated by central differences except at boundaries where one sided differences to the interior are employed. The Jacobian of the transformation  $\tilde{J}$  is

$$\begin{aligned} \tilde{J} = & x_\xi (y_\eta z_\psi - y_\psi z_\eta) + y_\xi (z_\eta x_\psi - x_\eta z_\psi) \\ & + z_\xi (x_\eta y_\psi - x_\psi y_\eta) \end{aligned} \quad (7a)$$

$$\equiv x_\xi \tilde{\xi}_x + y_\xi \tilde{\xi}_y + z_\xi \tilde{\xi}_z \quad (7b)$$

As directly interpreted equations (1), (6) and (7a) describe a finite volume method with (6) the cell face area and (7a) the volume. A finite (divided) difference upwind method such as is implemented here is obtained by dividing the interval averaged metrics by one sided difference cell volumes as given by equations like (7b) for each coordinate direction.

### Viscous Fluxes

The viscous terms of the flux vectors

$$\begin{aligned} \sigma_{xx} &= 2(\mu + \mu_r)(u_x - (u_x + v_y + w_z)/3) \\ \sigma_{yy} &= 2(\mu + \mu_r)(v_y - (u_x + v_y + w_z)/3) \\ \sigma_{zz} &= 2(\mu + \mu_r)(w_z - (u_x + v_y + w_z)/3) \\ \tau_{xy} &= \tau_{yx} = (\mu + \mu_r)(u_y + v_x) \\ \tau_{yz} &= \tau_{zy} = (\mu + \mu_r)(v_z + w_y) \\ \tau_{xz} &= \tau_{zx} = (\mu + \mu_r)(u_z + w_x) \end{aligned}$$

are second-order central differences in space and first-order implicit in time. These terms are treated with the Baldwin-Lomax<sup>11</sup> thin layer approximation.

When turbulence effects are present, they are presently modeled with the well known Baldwin and Lomax<sup>11</sup> algebraic mixing length model. The Baldwin-Lomax algebraic model defines an inner and outer layer formulation for the turbulent eddy viscosity in wall bounded shear layers, while only the outer layer is used for free shear layers and wakes. The main advantage of this model is that the velocity and length scales are easily defined and the model provides reasonable predictions. This model has been modified following the ideas of Bradshaw<sup>12</sup> for near wake flows, by setting a lower bound value for the wake law eddy viscosity as a function of the maximum viscosity value across the wake. This turbulence model has been used effectively to simulate 2-D/axisymmetric wakes and jet flows<sup>13,14,15</sup>. The flow of the present application around the forebody reentry vehicle at high altitude is essentially laminar. The turbulence model incorporated in the code would be useful in the simulation of the wake region or in aerodynamics problems at lower altitudes.

### Inviscid Fluxes

The inviscid flux terms of equation (1) are approximated with CSCM flux difference eigenvector splitting in an extension of the approach of reference 5. First order upwind spatial differencing is unconditionally stable with backward Euler pseudo-time iteration. For higher order upwind spatial differences, we incorporate flux limiting schemes of Yang, Lombard and Bardina<sup>19</sup>.

The CSCM-S method<sup>6,7</sup>, which is a (globally) single data level relaxation technique, is employed in marching along the  $\xi$ -direction. Within a  $\xi$  constant plane at each marching step the implicit equations are relaxed using the pseudo time dependent CSCM method which is a two data level relaxation technique employing DDADI approximate factorization in the  $\psi$  and  $\eta$  directions. The resulting implicit method of planes with one (additional) inner iteration at each spatial ( $\xi$ ) marching step provides a faster convergence of the solution for nonlinear systems of equations. While the processing time per grid point per iteration is increased, the number of total iterations is substantially decreased; especially when the  $\xi$ -direction is aligned with the main flow direction. Of equal importance as we shall discuss in a later section, this method also provides a substantial improvement in efficiency of data management of large 3-D data bases and is fully vectorizable.

Each of the flux difference vectors expressed in curvilinear coordinates is split according to the direction of the characteristic wave propagation by using the locally one dimensional similarity transformation that diagonalizes the transformation matrix  $\tilde{A}$  of the flux difference vector  $\Delta F$  by the conservative variables  $q$ , through the relations

$$\Delta F \equiv \tilde{A} \Delta q \equiv \overline{M} \overline{T} D \overline{T}^{-1} \widetilde{M}^{-1} \Delta q \quad (8)$$

where  $\overline{M}$  is the transformation matrix of the primitive variable differences into the conservative variable differences,

$$\overline{M} = \begin{pmatrix} 1 & 0 & 0 & 0 & 0 \\ \overline{u} & 1 & 0 & 0 & 0 \\ \overline{v} & 0 & 1 & 0 & 0 \\ \overline{w} & 0 & 0 & 1 & 0 \\ \frac{\overline{u}^2 + \overline{v}^2 + \overline{w}^2}{2} & \overline{u} & \overline{v} & \overline{w} & 1 \end{pmatrix}$$

and  $\overline{T}^{-1}$  is the transformation matrix of the primitive variable differences into the char-

acteristic variable differences,

$$\bar{T}^{-1} = \begin{pmatrix} -\frac{1}{\bar{\rho}} & 0 & 0 & 0 & \frac{1}{\gamma \bar{P}} \\ 0 & \bar{x}_\eta' & \bar{y}_\eta' & \bar{z}_\eta' & 0 \\ 0 & \bar{x}_\psi' & \bar{y}_\psi' & \bar{z}_\psi' & 0 \\ 0 & \bar{\xi}_x & \bar{\xi}_y & \bar{\xi}_z & \frac{1}{\gamma \bar{P}} \\ 0 & \frac{\bar{\xi}_x}{\bar{\rho} \bar{c}} & \frac{\bar{\xi}_y}{\bar{\rho} \bar{c}} & \frac{\bar{\xi}_z}{\bar{\rho} \bar{c}} & \frac{1}{\gamma \bar{P}} \\ 0 & -\frac{\bar{\xi}_x}{\bar{\rho} \bar{c}} & -\frac{\bar{\xi}_y}{\bar{\rho} \bar{c}} & -\frac{\bar{\xi}_z}{\bar{\rho} \bar{c}} & \frac{1}{\gamma \bar{P}} \end{pmatrix}$$

where the upper prime denotes

$$\bar{x}_\eta' = \bar{x}_\eta / \sqrt{\bar{x}_\eta^2 + \bar{y}_\eta^2 + \bar{z}_\eta^2},$$

$$\bar{\xi}'_x = \bar{\xi}_x / \sqrt{\bar{\xi}_x^2 + \bar{\xi}_y^2 + \bar{\xi}_z^2};$$

similarly, in all the other variables. The volumetric internal energy  $P \equiv p/(\gamma - 1)$  is a primitive variable of the formulation.

In equation (8), to effect the eigenvector splitting the unit matrix is split into three complementary  $D^+$ ,  $D^-$ , and  $D^0$  diagonal component matrices. The diagonal elements of these matrices are 0's or 1's according to the propagation direction of the characteristic waves, as given by the sign of the eigenvalues of the transformation matrix  $\tilde{A}$ . Thus  $D^+$  has 1's only on the diagonal coefficients of the rows corresponding to the rows of  $\tilde{A}$  with positive eigenvalues;  $D^-$  has 1's only on the diagonal coefficients corresponding to negative eigenvalues, while  $D^0$  is the complementary matrix for zero eigenvalues. This matrix  $D^0$  which is not separately identified in other numerical methods is employed to increase robustness and stability. The eigenvalues for the fluxes, e.g. in the  $\xi$ -direction are

$$\bar{W}^\xi, \quad \bar{W}^\xi + \bar{\xi} \bar{c}, \quad \bar{W}^\xi - \bar{\xi} \bar{c}, \text{ where} \quad (9)$$

$$\bar{W}^\xi = (\bar{\xi}_x \bar{\rho} \bar{u} + \bar{\xi}_y \bar{\rho} \bar{v} + \bar{\xi}_z \bar{\rho} \bar{w}) / \bar{\rho} \quad (10)$$

is the component of the contravariant averaged velocity, .

$$\bar{\xi} = (\bar{\xi}_x^2 + \bar{\xi}_y^2 + \bar{\xi}_z^2)^{1/2}, \text{ and} \quad (11)$$

$$\bar{c} = \bar{\gamma} \bar{p} / \bar{\rho} \text{ is the average sound speed.} \quad (12)$$

Consequently, the flux difference vector of equation (8) is split as

$$\Delta F \equiv \Delta F^+ + \Delta F^- \equiv (\tilde{A}^+ \Delta + \tilde{A}^- \Delta) q \quad (13)$$

where

$$\tilde{A}^\pm = \overline{M} \overline{T} D^\pm \overline{T}^{-1} \widetilde{M}^{-1} \quad (14a)$$

and  $\Delta$  is the forward-difference operator. Note the zero eigenvalue makes no contribution to the right hand side flux difference.

By analogy to the well known result for the scalar advection equation, unconditionally stable Euler implicit methods are constructed of the flux difference split pieces by upwind forward differencing with pieces associated with negative eigenvalues and, similarly, backward differencing pieces with positive eigenvalues.

To improve the diagonal dominance we impose the term

$$\tilde{A}^0 = \overline{M} \overline{T} D^0 \overline{T}^{-1} \widetilde{M}^{-1} \quad (14b)$$

on the diagonal of the left hand side. The method is well-posed in the case where the magnitude of any eigenvalue is zero; in these cases the approximation, effectively asserts that the characteristic quantity associated with a zero advective eigenvalue doesn't change<sup>17</sup>. The effectively frozen eigenfunction is found to make the system more stable and produces smooth solutions particularly through strong captured shock transitions.

### 3-D DDADI Implicit Diagonally Dominant Factorization

For computational efficiency, multi-dimensional linearized block implicit schemes employ approximate factorization of the left-hand side matrices to permit solving coupled matrix equations in one family of coordinates at a time.

The matrices corresponding to zero eigenvalues and that are added to  $I$  on the left hand side are shown in the relationships described below. Then, the 3-D unfactored system sketched as a first order method on the right hand side is

$$(I + A^0 + L) \delta q = -Lq \quad (15)$$

where the operators  $L$  and  $A^0$  are defined as

$$L = L_\xi + L_\eta + L_\psi \quad (16a)$$

$$A^0 = \tilde{A}_\xi^0 + \tilde{A}_\eta^0 + \tilde{A}_\psi^0 \quad (16b)$$

and

$$L_\xi = \tilde{A}_\xi^+ \nabla_\xi + \tilde{A}_\xi^- \Delta_\xi \quad (17a)$$

$$L_\eta = \tilde{A}_\eta^+ \nabla_\eta + \tilde{A}_\eta^- \Delta_\eta \quad (17b)$$

$$L_\psi = \tilde{A}_\psi^+ \nabla_\psi + \tilde{A}_\psi^- \Delta_\psi \quad (17c)$$

The 3-D diagonal-dominant approximate factorization DDADI<sup>5</sup> of the unfactored implicit upwind matrix equations is used to solve the system of equations. The resulting relaxation scheme for the method of planes is written as:

$$(I + A^0 + A_\xi + L_\eta + L_\psi) \delta q = -L^{n,n+1} q \quad (18)$$

where the absolute value matrix operator  $A_\xi$  on the diagonal is defined as

$$A_\xi = \tilde{A}_\xi^+ - \tilde{A}_\xi^- \quad (19)$$

The missing left hand side contribution of the off-diagonal matrix operator  $L_\xi - A_\xi$  are operationally included in the right-hand-side of equation (18) in the updated data of the symmetric pair of space marching sweeps<sup>6</sup>. Equation (18) is solved on each plane in the forward and backward space marching sweeps on alternating time steps, and the matrix operator  $L^{n,n+1}$  indicates that the data belonging to all previously computed planes are already updated.

In solving equation (18), the DDADI approximate factorization of the left-hand-side of equation (18) in the other two coordinate directions leads to the following block tridiagonal equation sequence:

$$(D + L_\eta - A_\eta) \delta q^* = -L^{n,n+1} q \quad (20)$$

$$(D + L_\psi - A_\psi) \delta q = -D \delta q^* \quad (21)$$

with

$$q^{n+1} = q^n + \delta q^n \quad (22)$$

and where the diagonal matrix operator  $D$  is defined as

$$D = I + A^0 + A_\xi + A_\eta + A_\psi \quad (23)$$

Observe that the absolute values of the eigenvalues for all coordinate directions are in the diagonally dominant matrix  $D$ , equations (20) and (21).

The Newton-Raphson inner iteration is applied by setting up the equations, solving and updating the base data at each plane twice during the forward and backward sweep procedure. This inner iteration is central to the improvement in fast rate of convergence of the solution of the nonlinear system of equations. The nonlinearities of the Navier-Stokes equations are better approximated in the updated locally active matrices, and the characteristic waves are propagated more accurately<sup>6</sup>.

#### Boundary Conditions

Implicit characteristic boundary procedures based on the approach of reference 5 are applied at each boundary where at least one characteristic wave propagates from the

boundary toward the interior of the computational domain. The boundary approximations are added as system of equations similar to the one for interior grid points of equations (18); except for the absence of convection matrices  $\tilde{A}^+$  at left boundaries and  $\tilde{A}^-$  at right boundaries which are replaced by local transformation matrices, similar to  $A^0$ , that contain the linear representations of the characteristic variables and auxiliary (imposed) boundary conditions in terms of conservative variables.

For supersonic freestream inflow conditions such as the outer boundary of reentry vehicles, the conservative flow variables are properly frozen. For supersonic outflow conditions, the conservative variables are properly extrapolated, i.e. calculated in the solution procedure, from the interior domain. For subsonic outflow, such as the one inside of the boundary layer zone, invariance in the static pressure is invoked by the solution procedure differencing toward the outflow boundary; however, the pressure field is allowed to appropriately relax since the solution procedure is also applied differencing along the outflow boundary. For viscous wall boundaries, no-slip conditions are applied and/or specified blowing/suction mass rates, together with specified wall temperature and/or adiabatic wall conditions. At symmetry planes, implicit symmetric approximations of the flux contributions beyond the boundary are imposed by symmetry relations based on the interior procedure toward the boundary.

#### Data Storage and Management

Three-dimensional numerical simulations often require large data bases of the order of few to several million words of storage. Due to the single data level relaxation technique and with recomputed metrics, the present method requires only eight variables per grid point, corresponding to the three coordinate directions and the five dependent variables. For large data bases on the CRAY-XMP computer that we have been using, the global arrays are stored in SSD solid-state devices. These devices have a fast transfer rate to the central memory of the vector processors where our method operates on only a few (five for the second order method)  $\xi$  data planes at a time. In the absence of the single level technique, at least five other (residual) variables with total grid dimensions will be required. Other variables may also be stored in order to avoid repetitive and unnecessary computation, particularly the nine metric coefficients and one Jacobian of the coordinate transformation.

With first order differencing in the  $\xi$ -direction, such as is implemented at present, the  $\xi$  sweeps require loading the data of planes  $J - 1$ ,  $J$ , and  $J + 1$  into central memory in order to process the data of plane  $J$ . In coding, the computation of the flux terms and matrix coefficients are fully vectorized in the  $\xi$  plane. The boundary conditions and solvers are also vectorized. Once the data of plane  $J$  is updated, this new data is stored, and the data of plane  $J + 2$  (on a forward sweep) is loaded into central memory in order to advance the data of plane  $J + 1$ . Thus, the complete forward  $\xi$  sweep requires loading the data base only once into central memory, and so does the backward  $\xi$  sweep.

### Initial Conditions

Appropriate initialization of the three-dimensional data is required in order to obtain convergence in comparatively few numerical iterations. In present work, solutions were first obtained for the case of 3-D axisymmetric flow with the 2-D/axisymmetric flow code<sup>5</sup>. The 3-D solutions are obtained within a few hundred iterations with about  $9 \cdot 10^{-5}$  cpu seconds per iteration and per grid point. This is a reasonable fast processing time considering that this is DDADI diagonal-dominant approximate factorization scheme. Then the solution is run with the 3-D code, changing only the free stream flowfield conditions, and the solution is obtained within N complete alternating sweeps where N is about half of the grid points in the streamwise direction. The three dimensional solutions relaxed in about 60 global iterations and about an hour of CPU time. Simpler initialization procedures, e.g. based on approximate shock fitting, can be similarly effective.

### Numerical Results

Numerical results of the hypersonic flow around a reentry vehicle (RV) are now presented. The geometry of the vehicle is a sphere-cone-cylinder-flare body. This geometry has previously been treated as Case 4 of Kim and Lewis<sup>18</sup>. Each part of the cone, cylinder, and flare section was 10 nose-radii axial length with a half angle of 16° in the cone surface and a half angle of 12° in the flare surface. The free stream Mach number is 22, the Reynolds number is  $10^5$ , Prandtl number is 0.7, and the ratio of specific heats  $\gamma=1.4$ . A cold wall boundary condition was applied with  $T_w/T_\infty = 7$ .

Figures 1a and 1b show different views of the  $64 \times 31$  point surface mesh on the reentry vehicle. The computational mesh has 64 points in the streamwise direction, 47 points from the body wall toward the outer boundary, and 31 points in the circumferential direction. The mesh has been constructed by using efficient 2-D algebraic procedures<sup>22</sup> based on transfinite interpolation in the upper and lower azimuthal symmetry planes, shown in Figure 1c, and a similar procedure with rotation between these two planes in order to define the remaining grid planes, as is shown in Figure 1d. Figure 1d shows a projection normal to the axis of the body of the computational mesh plane in the middle of the flare section. This simple procedure is very effective for this regular geometry to define the grid with minimum distortions and gives an excellent resolution around the body geometry and corner singularities. The grid lines are normal to the body wall and follow the general geometry of the bow shock.

Firstly, Figures 2a, 2b, and 2c show contour plots of Mach number, normalized pressure, and density of the hypersonic axisymmetric flow with 0° of angle of attack along a streamwise plane. The pressure is normalized with its free stream value. The bow shock is well captured and the contour lines in the shock layer are smooth and free of oscillations and/or instabilities. The expansion waves generated at the cone-cylinder corner and the weak oblique compression shock generated in the cylinder-flare corner are well captured by the method as shown in the pressure contours. The non-alignment of the grid with the bow shock is reflected as some small changes in the shock distribution, as well as, in the lower resolution in the flare section. The use of adaptive grid techniques should produce

optimal results in this kind of simulation.

In order to test the numerical results, we show in Figures 3a, 3b, and 3c similar contour plots to those of Figures 2, but obtained with the 2-D code for 3-D axisymmetric flows. The agreement is excellent between the flow contours of the 3-D and the axisymmetric 3-D simulations. The external bow shock, the expansion fan, and recompression shock are almost identical in both simulations. Minor differences can be seen in the leeward side of the cylinder-body section.

Figures 4a, 4b, and 4c show the contour plots of Mach number, normalized pressure, and density of the hypersonic flow at  $10^\circ$  of angle of attack along the bisymmetry plane. This numerical solution was obtained after running 60 global iterations or complete alternating sweeps over the axisymmetric solution. The residuals of the equation of motions decreased at least 3 orders of magnitude and the solution was converged. The flow structures are well captured and the contour lines are smooth and free of oscillations and/or instabilities. The expansion waves generated at the cone-cylinder corner and the weak oblique compression shock generated in the cylinder-flare corner are well captured by the method as shown in the pressure contours. Also evident is the inflection of the bow shock with the interaction of the expansion fans off the cone-cylinder junction. The pressure and density contours show a normal section of the recompression shock off the cylinder-flare junction.

Figure 5a shows the projection of the surface body mesh onto the bisymmetry plane, while Figure 5b show the contour plot of the normalized pressure on this plane. The effect of the free stream angle of attack on the pressure distribution is clearly defined in this Figure 5b, the highest contour values are on the sphere surface in the windward side and the smallest contour values are on the cylinder section in the leeward side. Figure 6a shows the surface pressure coefficient versus distance along the body surface. The horizontal axis of this plot is centered on the intersection of the axis of symmetry of the RV with the surface of the sphere section. The symbols show the pressure coefficients at  $10^\circ$  angle of attack along the body surface at every  $15^\circ$  from the bisymmetry plane, while the solid line shows the pressure coefficient at  $0^\circ$  angle of attack. Figure 6b shows a section of Figure 6a of the pressure distribution along the sphere-body section. The effects of the free stream angle of attack is well captured. There is some lack of smoothness near the pole of the grid topology due to an inconsistency of the grid spacing with the cross pole difference scheme that does not solve at the pole. The pole should have been "buried" at half cell spacing in the mesh.

Figures 7 show normalized pressure contours of cross sectional mesh planes projected onto the normal plane to the axis of body symmetry. Figures 7a, 7b, and 7c correspond to midplane section of the cone, cylinder, and flare sections, respectively, at  $10^\circ$  of angle of attack. On the other hand, Figure 7d correspond to midplane section of the flare section at  $0^\circ$  of angle of attack. Similarly, Figures 8 show the density contours corresponding to the respective Figures 7. These figures show the three-dimensionality of the flow structures, the development of the bow shock, the 3-D zone of expansion fan, and 3-D zone of recom-

pression shock. The complexity of the flow is shown to be well captured by the CSCM3D numerical method.

#### Concluding Remarks

The 3-D CSCM upwind compressible Navier-Stokes algorithm has been improved and extended to simulate external hypersonic flows at angle of attack. The method combines the best features of storage and processing efficiency of PNS space marching procedures with the generality of time dependent techniques to solve flows with elliptic and streamwise separated zones. The 3-D DDADI diagonal-dominant approximate factorization, together with well posed implicit boundary approximations, and the frozen eigenfunction approximation at zero eigenvalue crossings provide robust stability and fast relaxation to steady state. Numerical results for Mach 22 flow at 0° and 10° angle of attack of a sphere-cone-cylinder-flare reentry vehicle are presented. The numerical results are consistent with axisymmetric simulations and with previous experience in external hypersonic flows.

#### References

1. Anderson, J.D.: "A Survey of Modern Research in Hypersonic Aerodynamics," AIAA-84-1578, June 1984.
2. Bardina, J., and Lombard, C.K.: "Three Dimensional Hypersonic Flow Simulations with the CSCM Implicit Upwind Navier-Stokes Method," AIAA-87-1114-CP, June 1987.
3. Lombard, C.K. and Nagaraj, N.: "Extensions of the CSCM Upwind Methodology for Nonequilibrium Reacting Gas Flows," *International Symposium on Computational Fluid Dynamics-Sydney*, August 1987.
4. Lombard, C.K., Raiszadeh, Farhad and Bardina, Jorge: "Efficient, Vectorizable Upwind Implicit Relaxation Algorithm for Three-Dimensional Gasdynamics," Presented at the SIAM Spring Meeting, Pittsburgh, PA, June 1985.
5. Lombard, C.K., Bardina, J., Venkatapathy, E. and Oliger, J.: "Multi-Dimensional Formulation of CSCM - An Upwind Flux Difference Eigenvector Split Method for the Compressible Navier-Stokes Equations," AIAA-83-1895, July 1983.
6. Lombard, C.K., Venkatapathy, E. and Bardina, J.: "Universal Single Level Implicit Algorithm for Gasdynamics," AIAA-84-1533, 1984.
7. Lombard, C.K., Bardina, J., and Venkatapathy, E.: "AOTV Bluff Body Flow - Relaxation Algorithm," published in *Thermal Design of Aeroassisted Orbital Transfer Vehicles*, ed. by H.F. Nelson, Vol. 96 of Progress in Astronautics and Aeronautics, 1985.
8. Bardina, J. and Lombard, C.K.: "Three Dimensional CSCM Method for the Compressible Navier-Stokes Equations with Application to a Multi-Nozzle Exhaust Flow-field," AIAA-85-1193, July 1985.
9. Nagaraj, N., Lombard, C.K. and Bardina, J.: "Navier-Stokes Simulation of 3-D Hypersonic Equilibrium Air Flow," abstract submitted for the AIAA Thermophysics, Plasmadynamics and Lasers Conference at San Antonio, Texas, 1988.

10. Bardina, J., Venkatapathy, E., and Lombard, C.K.: "Two Dimensional and Ax-symmetric Heat Transfer Results with the CSCM-S Upwind Implicit Algorithm," published in *Thermophysical Aspects of Re-entry Flows*, ed. by J.N. Moss and C.D. Scott, Vol. 103 of Progress in Astronautics and Aeronautics Series, AIAA, 1986.
11. Baldwin, B.S. and Lomax, H.: "Thin Layer Approximation and Algebraic Model for Separated Turbulent Flows," AIAA 73-257, 1973.
12. Bradshaw, P.: "Prediction of the Turbulent Near Wake of a Symmetric Airfoil," *AIAA J.*, Vol. 8, p.1507, 1970.
13. Lombard, C.K., Luh, R.C.-C., Nagaraj, N., Bardina, J. and Venkatapathy, E.: "Numerical Simulation of Backward Step and Jet Exhaust Flows," AIAA-86-0432, January 1986.
14. Bardina, J., Venkatapathy, E., Nystrom, G. and Lombard, C.K.: "CSCM Methodology for Cavity Flow Design in a Supersonic Wedge Flow," AIAA-87-0518, January 1987.
15. Venkatapathy, E., Lombard, C.K., Bardina, J. and Luh, R.C.-C.: "Accurate Numerical Simulation of Supersonic Jet Exhaust Flow with CSCM on Adaptive Overlapping Grids," AIAA-87-0465, January 1987.
16. Yang, J.Y., Lombard, C.K. and Bardina, J.: "Implicit TVD Schemes for the Euler Equations with Bidiagonal Approximate FActorization," *International Symposium on Computational Fluid Dynamics, Tokyo, Japan*, Vol. 1, pp. 239-250, 1985.
17. Lombard, C.K.: "Conservative Supra-Characteristics Method for Splitting the Hyperbolic Systems of Gasdynamics for Real and Perfect Gases," NASA CR-166307, 1982.
18. Kim, M.D., and Lewis, C.H.: "Computation of Hypersonic Viscous Flow Past General Bodies at Angle of Attack and Yaw," AIAA-82-0225, January 1982.
19. Luh, R. C-C., Nagaraj, N., and Lombard, C.K.: "Simplified Algebraic Grid Generation in Patched Mesh Systems," AIAA-87-0200, January 1987.

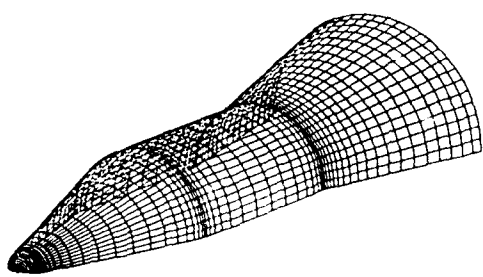


Figure 1a. 3-D view of surface mesh of sphere-cone-cylinder-flare reentry vehicle body.

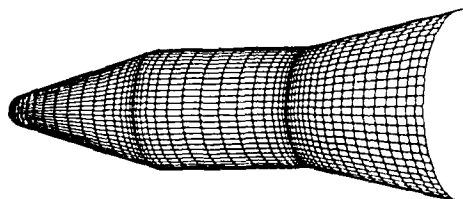


Figure 1b. 3-D view of surface RV mesh.

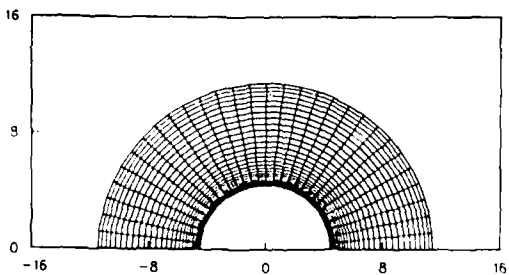


Figure 1d. Normal projection of cross sectional mesh in flare-body sector.

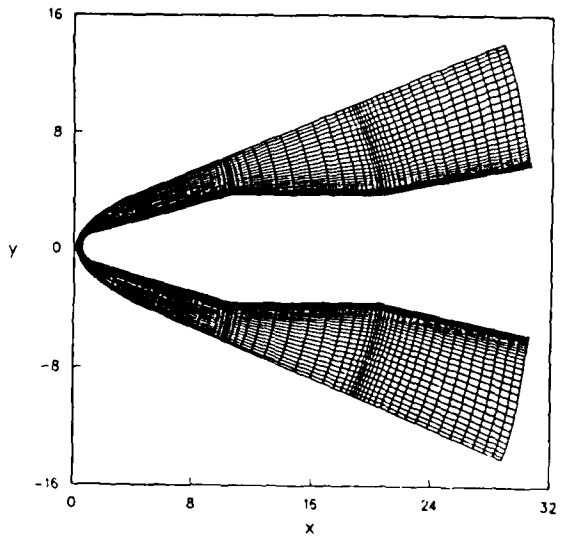


Figure 1c. Computational mesh on bisymmetry plane of RV vehicle.

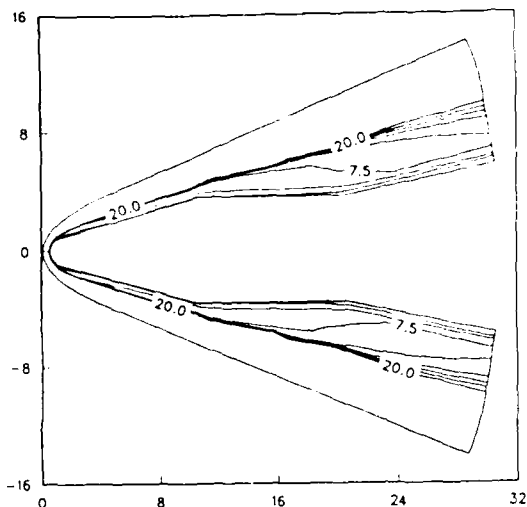


Figure 2a. Mach contour lines on bisymmetry plane. 3-D simulation of hypersonic axisymmetric flow.

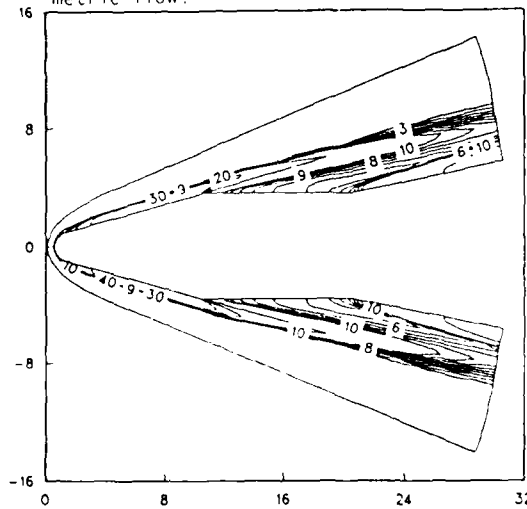


Figure 2b. Normalized pressure contour lines.

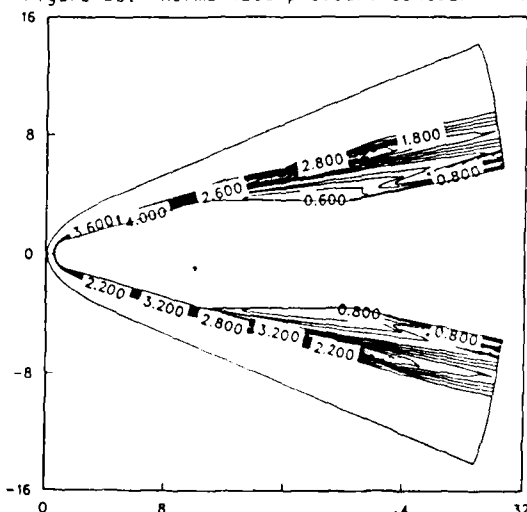


Figure 2c. Density contour lines.

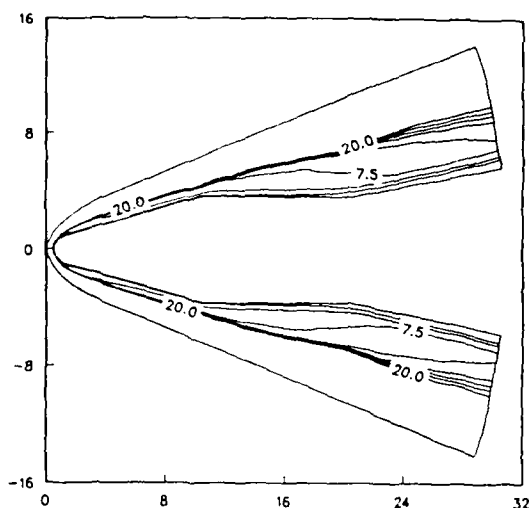


Figure 3a. Mach contour lines on bisymmetry plane. 2-D axisymmetric simulation.

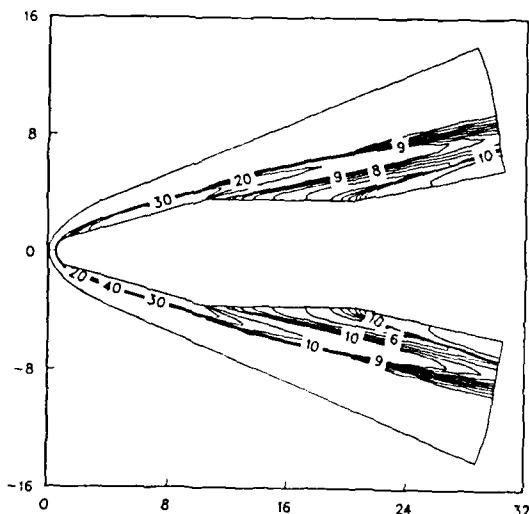


Figure 3b. Normalized pressure contour lines.

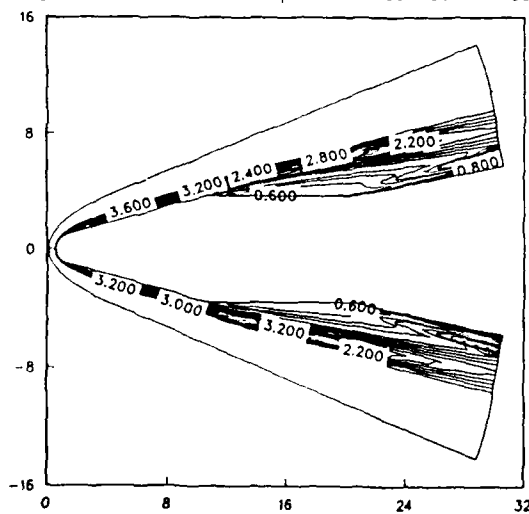


Figure 3c. Density contour lines.

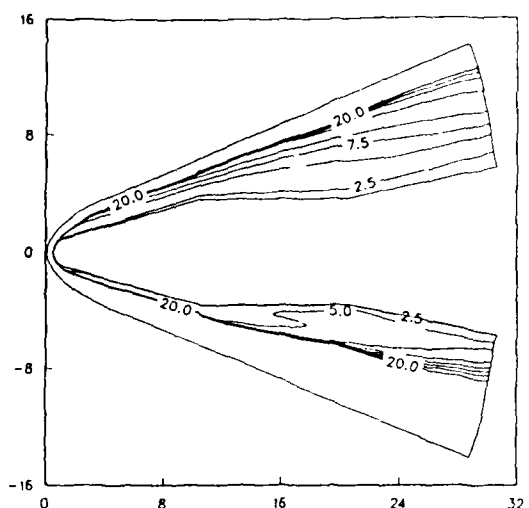


Figure 4a. Mach contour lines on bisymmetry plane. 3-D simulation of hypersonic flow at 10° angle of attack.

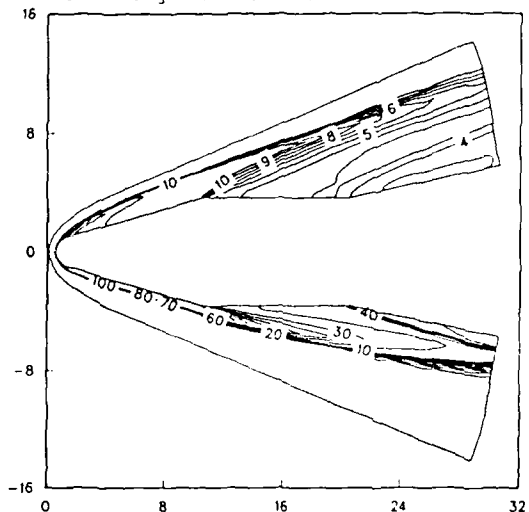


Figure 4b. Normalized pressure contour lines.

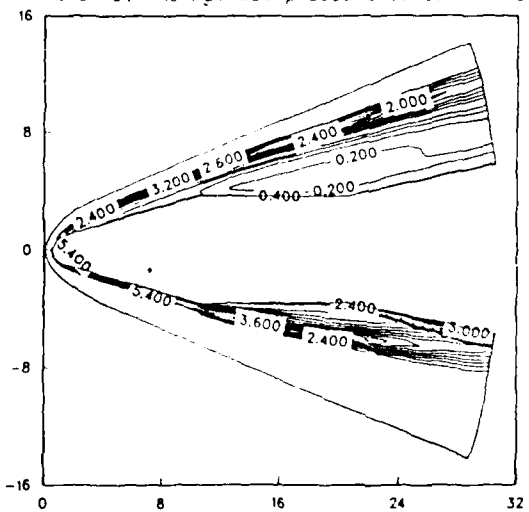


Figure 4c. Density contour lines.

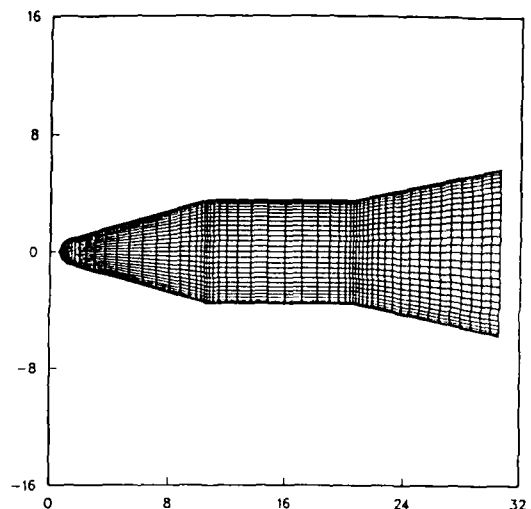


Figure 5a. Surface mesh body projected onto bisymmetry plane.

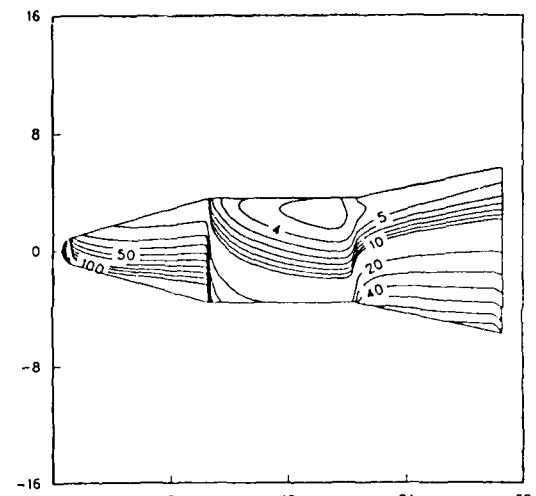


Figure 5b. Normalized pressure contour lines of hypersonic flow at 10° angle of attack, corresponding to figure 5a.

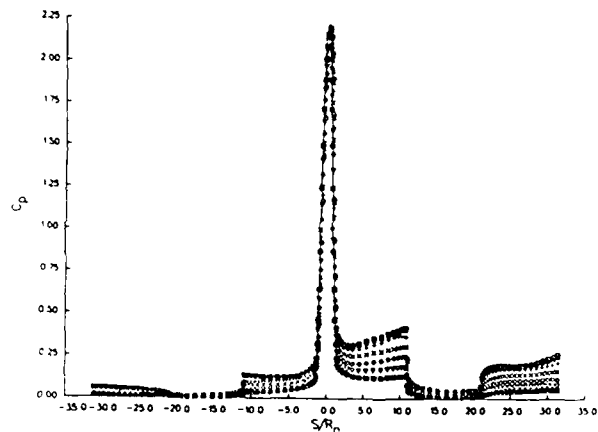


Figure 6a. Surface pressure coefficient along RV body. Symbols show predictions along planes at 0°, 15°, 30°, 45°, 60°, 75°, and 90° off the bisymmetry plane of hypersonic flow at 10° angle of attack. Solid line shows prediction of axi-symmetric flow at 0° angle of attack.

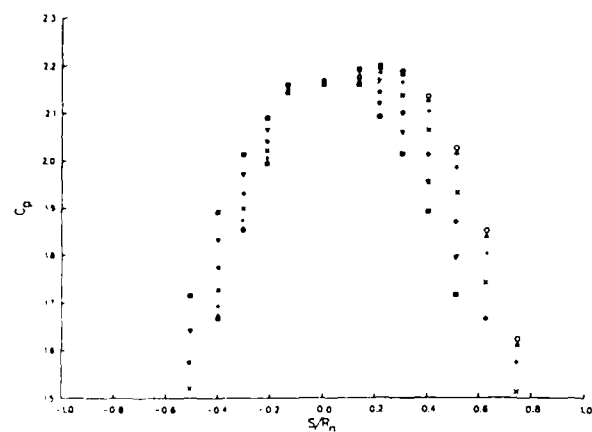


Figure 6b. Surface pressure coefficient along the sphere-body section. Symbols correspond to figure 6a.

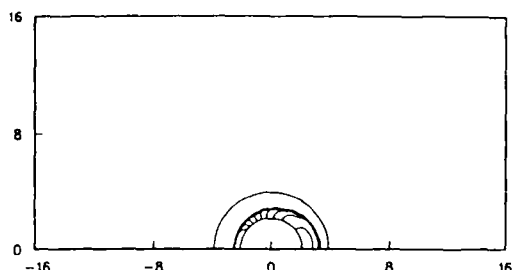


Figure 7a. Normalized pressure contour lines of hypersonic flow at  $10^\circ$  angle of attack, on cross sectional mesh midplane of cone-body section.

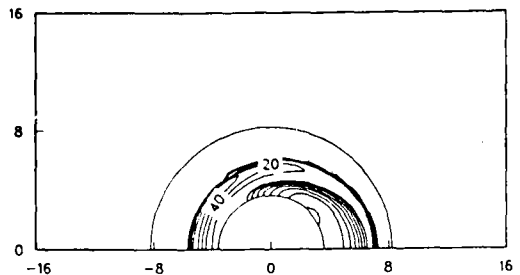


Figure 7b. Normalized pressure contour lines of hypersonic flow at  $10^\circ$  angle of attack, on cross sectional mesh midplane of cylinder-body section.

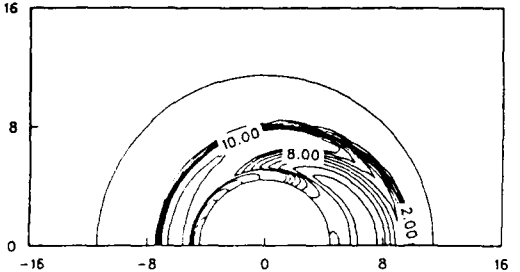


Figure 7c. Normalized pressure contour lines of hypersonic flow at  $10^\circ$  angle of attack, on cross sectional mesh midplane of flare-body section.

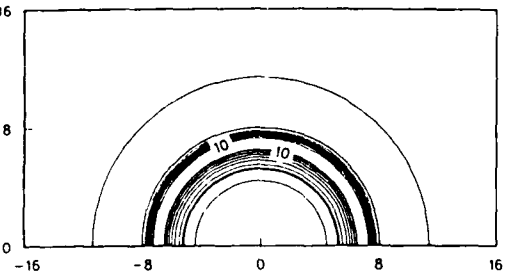


Figure 7d. Normalized pressure contour lines of axisymmetric hypersonic flow on cross sectional mesh midplane of flare-body section.

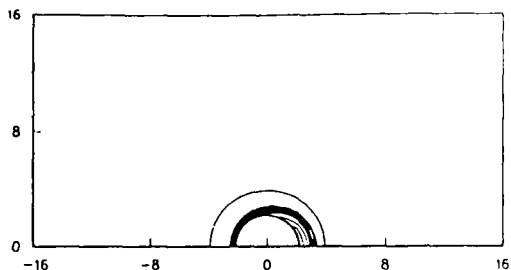


Figure 8a. Density contour lines, corresponding to figure 7a.

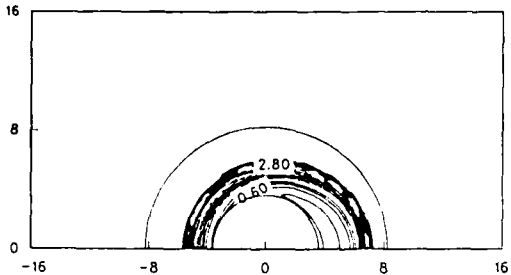


Figure 8b. Density contour lines, corresponding to figure 7b.

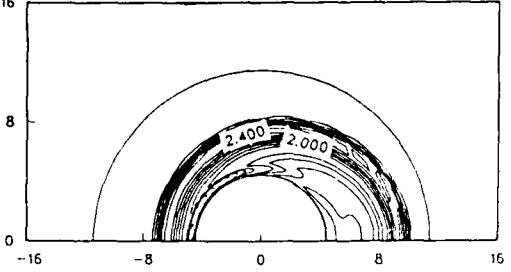


Figure 8c. Density contour lines, corresponding to figure 7c.

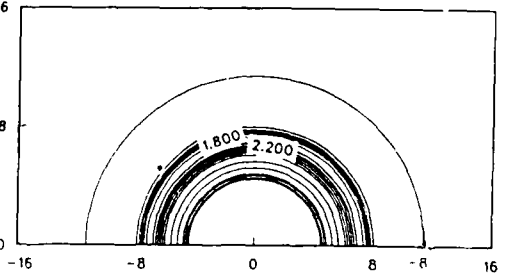


Figure 8d. Density contour lines, corresponding to the figure 7d.

## **7. Professional Personnel**

Professional researchers who were supported under and contributed to this project are  
Dr. Charles K. Lombard, Principal Investigator  
Professor Joseph Oliger, Consultant  
Dr. Jorge Bardina, Staff Scientist  
Dr. Ethiraj Venkatapathy, Staff Scientist  
Dr. J.Y. Yang, Research Scientist

## **8. Interactions**

The research described in this report has been partially presented in seven technical meetings in the U.S. and abroad. The research in simplified algebraic grid generation is partially described in Section 1 reference 2 of this annual report.

The solution adaptive grid work on multiple patch meshes has been given in a paper, Accurate Numerical Simulation of Supersonic Jet Exhaust Flow with CSCM on Adaptive Overlapping Grids, AIAA-87-0465, AIAA 25th Aerospace Sciences Meeting, Reno, NV, January 12-15, 1987. The work has also been presented in a talk by C.K. Lombard at the Second Nobeyama Workshop on Supercomputing in Fluid Dynamics, Nobeyama, Japan, September 7-10, 1987.

Work on the CSCM upwind method expressed as a finite volume method on node bounded cells in staggard grids has been partially presented in a paper, Accurate, Efficient and Productive Methodology for Solving Turbulent Viscous Flows in Complex Geometry, for the 10th International Conference on Numerical Methods in Fluid Dynamics, Beijing, China, June 23-27, 1986.

Work on nonlinearly stable high order biased upwind methods has been partially presented in a paper, Uniformly Second Order Accurate ENO Schemes for the Euler Equations of Gas Dynamics, AIAA-87-1166-CP, AIAA 8th Computational Fluid Dynamics Conference, Honolulu, Hawaii, June 9-11, 1987.

The CSCM shock capturing scheme with improved diagonal dominance through frozen eigenfunctions for zero eigenvalue crossings has been presented with application of 3-D hypersonic blunt body flow in the paper, Three Dimensional Hypersonic Flow Simulations with the CSCM Implicit Upwind Navier-Stokes Method, AIAA-87-1114-CP, AIAA 8th Computational Fluid Dynamics Conference, Honolulu, Hawaii, June 9-11, 1987.

Recent application of the combined algebraic grid generation and surface geometry definition tools with the segmented patched 2-D/axisymmetric CSCM Navier-Stokes solver (developed under AFOSR support) to the design modification of the throat region of the Mach 14 nozzle of the NASA-Ames 3.5 ft hypersonic tunnel are reported in the paper, Aerodynamic Design Modification of a Hypersonic Wind Tunnel Nozzle by CSCM with High Order Accuracy, AIAA-87-1896, AIAA/SAE/ASME/ASEE 23rd Joint Propulsion Conference, San Diego, CA, June 29-July 2, 1987.

## **9. New Discoveries**

The CSCM method on node bounded finite volume computational cells in a staggard grid is a new class of flux difference split upwind schemes.

FILMED  
58